

**Investigation of Selective Optical Properties of Si/SiO<sub>2</sub> Nanostructures  
Generated by Pulsed Laser Ablation As-Deposited and Post-treated**

by

Meisam Moghareh Abed

A thesis submitted to the  
School of Graduate and Postdoctoral Studies in partial  
fulfillment of the requirements for the degree of

**Master of Applied Science**

**in**

**Mechanical Engineering**

Faculty of Engineering and Applied Science

University of Ontario Institute of Technology (Ontario Tech University)

Oshawa, Ontario, Canada

May 2020

© Meisam Moghareh Abed, 2020

## THESIS EXAMINATION INFORMATION

Submitted by: **Meisam Moghareh Abed**

### **Master of Applied Science in Mechanical Engineering**

Thesis title: Investigation of Selective Optical Properties of Si/SiO<sub>2</sub> Nanostructures Generated  
by Pulses Laser Ablation As-deposited and Post-treated

An oral defense of this thesis took place on May 22, 2020 in front of the following examining committee:

#### **Examining Committee:**

Chair of Examining Committee      Dr. Martin Agelin-Chaab

Research Supervisor                  Dr. Amirkianoosh Kiani

Thesis Examiner                      Dr. Jana Abou-Ziki

Examining Committee member      Dr. Sayyed Ali Hosseini

The above committee determined that the thesis is acceptable in form and content and that a satisfactory knowledge of the field covered by the thesis was demonstrated by the candidate during an oral examination. A signed copy of the Certificate of Approval is available from the School of Graduate and Postdoctoral Studies.

## **ABSTRACT**

Silicon and its derivatives like SiO<sub>2</sub> are essential materials for industrial applications such as semiconductors, optoelectronics, and telecommunication. Optical properties of a large group of silicon/silica nanofibrous thin films are studied. A picosecond pulse laser was employed for indirect deposition of ablated silicon on glass substrates. Prominent parameters such as laser power, repetition rate, pulse duration, and scanning speed were changed to vary the structural and compositional properties of synthesized nanofibrous thin films. Transmission and specular reflection measurements along with material characterization techniques, Raman, FTIR XPS, and XRD were employed for better interpretation of the results. Three studies are included in this research. First, exploration of the effect of manufacturing parameters as frequency, power, pulse duration and scanning speed on optical properties of samples generated. By and large, an increase in the values for repetition rate and scanning speed produces a corresponding increase in optical data intensity, while an increase in power and pulse duration leads to a drop in the spectra. The results show that the degree of oxidation and the inherent porous structure is driving the light interaction in thin samples, as indicated by the changes in intensity or spectrum shape. The second study looks into the influence of post heat treatment on the optical properties of samples prepared by frequency variation. Samples were heated up to 400°C and 1000°C and cooled down to room temperature for measurements. The inverse relationship of annealing temperatures on Vis-range reflection spectra to increase and decrease the intensity was confirmed. These improvements are attributed to crystalline and amorphous lattice structures and elemental composition. The third study focuses on the emission of a heated sample, to 200°C and 350°C while data is collected at the elevated temperatures. Results show the emission amplifying effect of nanofibrous structure and its density as well as oxidation level at NIR (Near Infra-Red) range reflection.

**Keywords:** Transmission; Reflection; Silicon; Ablation; Emissivity

## **AUTHOR'S DECLARATION**

I hereby declare that this thesis consists of original work of which I have authored. This is a true copy of the thesis, including any required final revisions, as accepted by my examiners.

I authorize the University of Ontario Institute of Technology (Ontario Tech University) to lend this thesis to other institutions or individuals for the purpose of scholarly research. I further authorize University of Ontario Institute of Technology (Ontario Tech University) to reproduce this thesis by photocopying or by other means, in total or in part, at the request of other institutions or individuals for the purpose of scholarly research. I understand that my thesis will be made electronically available to the public.

Meisam Moghareh Abed

## STATEMENT OF CONTRIBUTIONS

Part of the work described in Chapter 3, Chapter 4 and Chapter 5 are either published or under consideration for publication as:

Abed, M.M., F. Gaspari, and A. Kiani, “*Optical properties of Si/SiO<sub>2</sub> nano structured films induced by laser plasma ionization deposition*”. Optics Communications, 2020: p. 125297

<https://doi.org/10.1016/j.optcom.2020.125297>

Abed, M.M., A. Kiani, “*The impact of heat treatment on optical reflectivity of laser induced Si/SiO<sub>2</sub> thin films*”, Journal of Solid Thin Films, Under review

Abed, M.M., A. Kiani, “*Emissivity Study of Hybrid Si/SiO<sub>2</sub> Nanostructures Synthesized by Picosecond Laser Pulses at Different Laser Scanning Speeds and Repetition Rates I performed the majority of the synthesis, testing of membrane materials, and writing of the manuscript*”, Journal of Nanomaterials , Under Review

## **ACKNOWLEDGEMENTS**

Firstly, I would like to express my gratitude to my advisor Dr. Amirkianoosh Kiani for the continuous guidance and motivation during this study. Next, my sincere thanks go to my wife and my parents for supporting me spiritually throughout the accomplishment of my research.

## TABLE OF CONTENTS

<b>Chapter 1. Introduction.....</b>	<b>1</b>
1.1 Silicon and Derivatives .....	1
1.2 Si-based thin films.....	1
1.2.1 Sacrificial Use of Porous Silicon in Microsystems.....	5
1.2.2 Porous Silicon-Based Sensing Microsystems .....	6
1.2.3 Porous Silicon Optical Biosensors.....	8
1.3 Highlights of Fabrication Methods .....	9
<b>Chapter 2. Experiments and Techniques.....</b>	<b>14</b>
2.1 Materials and Overview .....	14
2.2 Tools and Equipment .....	15
2.3 Characterization techniques .....	17
2.4 Statistical analysis .....	22
<b>Chapter 3. 1<sup>st</sup> Study: Laser nanofabrication parameter study.....</b>	<b>23</b>
3.1 Introduction .....	23
3.2 Sample preparation.....	23
3.3 Results and Discussion.....	24
3.4 Conclusion.....	36
<b>Chapter 4. 2<sup>nd</sup> Study: Post heat treatment of Si/SiO<sub>2</sub> thin films .....</b>	<b>37</b>
4.1 Introduction .....	37
4.2 Sample Preparation .....	37
4.3 Results and Discussion.....	38
4.4 Conclusion.....	45
<b>Chapter 5. 3<sup>rd</sup> Study: Thin film real-time emissivity research .....</b>	<b>46</b>
5.1 Introduction .....	46
5.2 Sample preparation.....	47
5.3 Results and Discussion.....	49
5.4 Conclusion.....	55
<b>Chapter 6. Outcome and Outlook .....</b>	<b>56</b>
6.1 Closing remark .....	56
6.2 Future Perspective .....	58
<b>References .....</b>	<b>59</b>
<b>Appendix .....</b>	<b>68</b>

## LIST OF TABLES

Table 1-1 Categories of pores [1] .....	2
Table 1-2 A multitude of routes to form porous silicon [1].....	3
Table 1-3 Porous silicon as a sacrificial layer.....	6
Table 1-4 Porous silicon sensing microsystems .....	7
Table 2-1 Thin films manufacturing factors .....	15
Table 3-1 Quantity and manufacturing variable .....	23
Table 3-2 Trends in Fig. 3-1, Fig. 3-2.....	26
Table 3-3 Average film thickness .....	31
Table 3-4 Peak power with parameter change .....	32
Table 4-1 Manufacturing parameters .....	38
Table 4-2 Produced samples .....	38
Table 5-1 Nanofabrication parameters and sample quantity .....	48

## LIST OF FIGURES

Fig. 1-1 Schematic representation for the structures of (a) crystalline silicon (c-Si) and (b) amorphous silicon (a-Si:H)[1] .....	2
Fig. 1-2 Current broad application areas of porous silicon under evaluation. Applications are arranged by the dominant physical form of porous silicon required. On the left-hand column, applications require primarily powders, on the right-hand column primarily chip-based layers. The central column applications utilize all three dominant forms: powders, membranes, and films [1].....	5
Fig. 1-3 Surface area enhancement by miniaturization, Reprinted from Sensors and Actuators,268, Paladya, A. Kiani, “Nano structured sensing surface: Significance in sensor fabrication”,Copyright (2018)with permission from Elsevier [80] .....	8
Fig. 1-4 Schematic of porous Si synthesis by a bottom-up approach, stain etching, and anodization [97] .....	10
Fig. 1-5 Schematic diagram of etching cell used for PSi formation by electrochemical etching [95] .....	11
Fig. 2-1 Schematic A) experiment set-up B) nanostructure formation [120] .....	14
Fig. 2-2 Pulsed laser setup with components and their arrangement.....	16
Fig. 2-3 Schematic drawing of an SEM instrumentation [107] .....	18
Fig. 2-4 Raman scattering spectroscopy facility [108] .....	19
Fig. 2-5 FTIR spectroscopy generic schematic [110] .....	20
Fig. 2-6 Schematic diagram of an XPS spectrometer [107] .....	21
Fig. 2-7 a generic X-ray scattering measurement .....	21
Fig. 2-8 Schematic of an XRD basic components .....	22
Fig. 3-1 Vis range transmission (A, C, E, G) and reflection (B, D, F, H)[120].....	24
Fig. 3-2 NIR range transmission (A,C,E,G) and reflection (B,D,F,H) [120] .....	25
Fig. 3-3 Vis range transmission (A,C,E,G) and reflection (B,D,F,H) normalized graph [120].....	27
Fig. 3-4 NIR range transmission (A,C,E,G) and reflection (B,D,F,H) normalized graph [120].....	28
Fig. 3-5 SEM images magnified at X20K of samples in four groups: (A,B,C) for power, (D,E,F) for frequency, (G,H,I) for pulse duration and (J,K,L) for speed changes [120] ...	29
Fig. 3-6 Average surface temperature of the target surface with P, Frq, Pd and SS samples against effective pulse numbers [120] .....	31
Fig. 3-7 Raman scattering spectra for groups of (A)P,(B)Frq,(C)Pd and (D)SS [120] .....	32
Fig. 3-8 FTIR spectra for groups of (A)P,(B)F[125]rq,(C)Pd and (D)SS [120].....	34
Fig. 4-1 Schematic experiment set-up (not to scale).....	37
Fig. 4-2 Typical SEM images of two groups of samples with low and high magnification (A,B typically show S11to S13 and C,D,typically shows S21 to S23) .....	39
Fig. 4-3 Vis range reflection spectrum for two sets of samples (A: Group1, B: Group2).40	
Fig. 4-4 Vis range reflectivity of two groups of samples (A:600kHz, B:1200kHz) with heat treatment.....	40
Fig. 4-5 XPS survey spectra of group1 samples, 600kHz, (A,C,E) and XPS narrow cut spectra and chemical state analysis for the Si 2p region at ~103 eV, (B,D,F).....	41

Fig. 4-6 XPS survey spectra of group2 samples, 1200kHz, (A,C,E) and XPS narrow cut spectra and chemical state analysis for the Si 2p region at ~103 eV, (B,D,F).....42

Fig. 4-7 O 1s XPS spectra before and after treatment for Group1 (A) and Group2(B) samples.....42

Fig. 4-8 XRD patterns of thin films with Si substrate (A) Magnified XRD spectrum of the thin film (B) for Group1 samples.....44

Fig. 4-9 XRD patterns of thin films with Si substrate (A) Magnified XRD spectrum of the thin film (B) for Group2 samples.....44

Fig. 5-1 Experimental setup: hot plate, spectroscopy, source light, and reflection probe .48

Fig. 5-2 Frequency varied samples with no distinguishable change in emission at 50°C .49

Fig. 5-3 Emission measured at 200°C and 350°C from frequency varied samples .....50

Fig. 5-4 SEM images of samples synthesized at A) 600kHz, B) 900kHz, C) 1200kHz ...51

Fig. 5-5 Raman spectra in the vicinity of Si/SiO<sub>2</sub> peak for frequency variation.....51

Fig. 5-6 Emission measured at 200°C and 350°C from frequency varied samples .....52

Fig. 5-7 SEM images of samples synthesized at A) 10mm/s, B) 100mm/s, C) 200mm/s.52

Fig. 5-8 Raman spectra in the vicinity of Si/SiO<sub>2</sub> peak for scanning speed variation .....53

## LIST OF ABBREVIATIONS

PLA	Pulsed Laser Ablation
ALD	Atomic Layer Deposition
a-Si	Amorphous Silicon
PSi	Porous Silicon
c-Si	Crystalline Silicon
MEMS	Micro Electro Mechanical System
MACE	Metal ion-assisted chemical etching
PL	Photo Luminescence
SEM	Scanning Electron Microscopy
FTIR	Fourier Transform Infra Red
XPS	X-ray Photoelectron Spectroscopy
XRD	X-ray Diffraction Analysis
SERS	Surface-Enhanced Raman Scattering

# Chapter 1.

## Introduction

### 1.1 Silicon and Derivatives

Silicon (Si) is abundant on earth and well established as an ideal platform for optoelectronics, communication, and microelectronic devices owing to its magnificent optical, electrical, and mechanical properties. Silicon dioxide, also known as silica, is an oxide of silicon with the chemical formula  $\text{SiO}_2$ , most commonly found in nature as quartz and various living organisms. In many parts of the world, silica is the major component of sand. It is one of the most complex and abundant families of materials, existing as a compound of minerals and as synthetic products. Notable examples include fused quartz, fused silica, silica gel, and aerogels. They are used in structural materials, microelectronics (as an electrical insulator), and as components in the food and pharmaceutical industries [1,2].

### 1.2 Si-based thin films

Si/SiO<sub>2</sub>-based thin films have been utilized in microelectromechanical system (MEMS)-based devices, antireflective surface structuring, and surface patterning of materials for biomedical applications. Solar cells with nc-Si (nanocrystalline silicon) layers owing to their photoconductive properties have proved to be an efficient and low-cost technology [1]. The nanostructured silicon, namely nanocrystalline Si (nc-Si), nanostructured amorphous Si (a-Si), nc-Si or a-Si embedded in the amorphous SiO<sub>2</sub> matrix (SiO<sub>x</sub>), nc-Si embedded in the Si<sub>3</sub>N<sub>4</sub> matrix (SiN<sub>x</sub>) and porous silicon (P-Si), exhibit intense fascinating visible and near infrared optical behaviors (Fig. 1-1) [2,3].

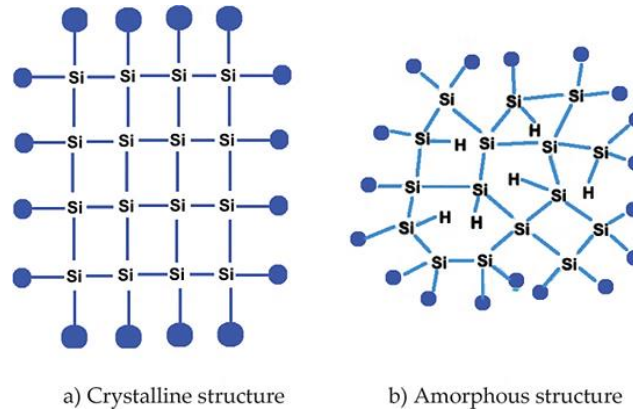


*Fig. 1-1 Schematic representation for the structures of (a) crystalline silicon (c-Si) and (b) amorphous silicon (a-Si:H)[1]*

Porous silicon (PSi) is a versatile nanomaterial that has been used in several applications such as optical switching, drug delivery, and sensors since its discovery in 1991 [3]. Porous silicon (PS) was first discovered by Uhlir in 1956, it is produced by the etching of Si wafers or powders in HF-based electrolyte [4]. Table 1-1 shows the nomenclature for categories of pores in silicon.

*Table 1-1 Categories of pores [1]*

Term	Pore diameter (nm)
Nanopore	Up to 100 nm
Macropore	Greater than 50 nm
Mesopore	2–50 nm
Micropore	Less than 2 nm

Table 1-2 illustrates the variety of processes (currently more than 40) now available to create different forms of porous silicon, arranged in approximately the chronological order they have been introduced. Historically, it was high levels of mesopores that were generated first using anodization (1) and stain etching (2) of electronic-grade crystalline silicon.

Table 1-2 A multitude of routes to form porous silicon [1]

Fabrication technique	Class of technique	Class of porosity	Early paper on technique
Anodization	Etching (wet)	Mesoporous	Uhlir (1956)[4]
Stain etching	Etching (wet)	Mesoporous	Archer (1960)[5]
Anodization	Etching (wet)	Macroporous	Theunissen (1972)[6]
Anodization	Etching (wet)	Microporous	Canham and Groszek (1992)[7]
Spark erosion	Etching (dry)	Mesoporous	Hummel and Chang (1992)[8]
Photoetching	Etching (wet)	Mesoporous	Noguchi and Suemune (1993)[9]
Laser ablation	Thermal	Mesoporous	Savin et al. (1996)[10]
Hydrothermal etching	Etching (wet)	Mesoporous	Chen et al. (1996) [11]
Metal ion-assisted chemical etching (MACE)	Etching (wet)	Mesoporous	Dimova-Malinovska et al. (1997)[12]
Galvanic etching	Etching (wet)	Mesoporous	Ashruff et al. (1999) [13]
Plasma deposition	Deposition	Mesoporous	Kalkan et al. (2000) [14]
Vapor etching	Etching (wet)	Mesoporous	Saadoun et al. (2002) [15]
Laser-induced plasma	Etching (dry)	Macroporous	Kabashin and Meunier (2002) [16]
Glancing angle deposition	Deposition	Mesoporous	Beydaghan et al. (2004) [17]
Melt gasification	Thermal	Macroporous	Nakahata and Nakajima (2004) [18]
Plasma hydrogenation	Deposition	Mesoporous	Abdi et al. (2005) [19]
Dealloying	Etching (wet)	Mesoporous	Fukatani et al. (2005) [20]
Templated plasma etch	Etching (dry)	Macroporous	Tian et al. (2005) [21]
Laser-induced silane decomposition	Deposition	Mesoporous	Voigt et al. (2005) [22]
Magnesiothermic reduction of silica	Conversion reaction	Mesoporous/ Microporous	Bao et al. (2007) [23]
Mechanochemical reduction	Conversion reaction	Mesoporous	Zheng et al. (2007) [24]
Milling/sintering	Mechanical	Macroporous	Jacobowicz et al. (2007) [25]
Sodiothermic reduction of silica gel and templated sintering	Conversion reaction	Macroporous	Kim et al. (2008) [26]
DRIE-UV lithography	Etching (dry)	Macroporous	Woldering et al. (2008) [27]
Femtosecond laser ablation	Thermal	Mesoporous	Mahmood et al. (2009) [28]
Ultrathin film annealing	Thermal	Mesoporous	Fang et al. (2010) [29]
Anodization (alkali)	Etching (wet)	Macroporous	Abburi et al. (2010) [30]

(Continued) Table 1-2

Fabrication technique	Class of technique	Class of porosity	Early paper on technique
Electrodeposition	Deposition	Mesoporous	Krishnamurthy et al. (2011) [31]
Ultrasonic etching	Etching (wet)	Mesoporous	Skorb et al. (2012) [32]
Carbothermal reduction of silica	Conversion reaction	Macroporous	Yang et al. (2012) [33]
Sacrificial template	Deposition	Mesoporous	Huang et al. (2013)[34]
Sodiothermic reduction of silica	Conversion reaction	Mesoporous	Wang et al. (2013) [35]
Magnetron sputtering	Deposition	Mesoporous	Godinho et al. (2013) [36]
Micromachining and wet etching	Etching (wet)	Macroporous	Deng et al. (2013) [37]
Platinum NP-assisted etching	Etching (wet)	Mesoporous	Li et al. (2013) [38]
Ion implantation	Irradiation	Macroporous	Stepanov et al. (2013) [39]
Templated silicon tetrachloride reduction	Conversion reaction	Mesoporous	Dai et al. (2014) [40]
Rochow reaction-based etching	Etching (dry)	Macroporous	Zhang et al. (2014) [41]
Dealloying in a metallic melt	Conversion reaction	Macroporous	Wada et al. (2014) [42]
Magnesium silicide decomposition	Conversion reactions	Mesoporous	Liang et al. (2015) [43]
Ion track template etch	Etching (wet)	Mesoporous	Kaniukov et al. (2016) [44]
Focused electron beam induced etching	Etching (dry)	Macroporous	Peer et al. (2016) [45]
Regenerative electroless etching	Etching (wet)	Mesoporous	Kolasinski et al. (2017) [46]

Twelve application domains are shown schematically for porous silicon in Fig. 1-2. Four electronic-based application areas on the right-hand column are the most developed of these categories. Those on the left-hand side utilize primarily porous silicon powders, and it is the medical domain that is currently receiving the most academic and industrial attention. In the central column lie many of the traditional applications for porous materials.



*Fig. 1-2 Current broad application areas of porous silicon under evaluation. Applications are arranged by the dominant physical form of porous silicon required. On the left-hand column, applications require primarily powders, on the right-hand column primarily chip-based layers. The central column applications utilize all three dominant forms: powders, membranes, and films [1]*

An updated literature survey shows various uses of porous silicon in individual microdevices and complex microsystems. The material has been used (a) as a silicon wafer processing tool wherein it is sacrificial (b) in a passive role where it can provide thermal or electrical isolation and (c) in an active role where it can perform several diverse functions. Examples of active functions available for microsystems include culturing cells, sensing, delivering drugs, providing sources of energy for micro actuators, or having a catalytic role in microelectrodes. [1-3]

### 1.2.1 Sacrificial Use of Porous Silicon in Microsystems

Macroporous silicon technology found its principal application in integrated microsystems as sacrificial layer: multilayered and suspended structures, such as bridges, membranes, and cantilevers, often require fabrication, almost always by isotropic etching and removing, by alkaline-based water solution, of a porous layer. The thickness of this layer can be up to 100  $\mu\text{m}$ , or more, which is very much greater with respect to those obtained by thin film deposition techniques ( $<10 \mu\text{m}$ ): in this sense, porous silicon passive layer is an exclusive

technology. There are some reported references of porous silicon sacrificial layers together with the functionalities of the resulting microsystems in Table 1-3.

*Table 1-3 Porous silicon as a sacrificial layer*

<b>Sacrificial structure</b>	<b>End product</b>	<b>Reference</b>
Freestanding film	Flow channels	Lang et al. (1994) [47]
Bridge	Flow sensor	Lang et al. (1995) [48]
Thin films, wires	Bolometer, anemometer	Steiner and Lang (1995) [49]
Cantilever	Micromachining	Bischoff et al. (1997) [50]
Wick	Wall of heat pipe	Holke et al. (1998) [51]
Cantilever	Accelerometer	Sim et al. (1998) [52]
3D plates	MEMS	Lammel and Renaud (2000) [53]
Membrane	Microelectrodes	Kalinowski et al. (2000) [54]
Cantilevers, disks	MEMS	Lee et al. (2000) [55]
Nanoporous structures	MEMS	Benecke and Splinter (2001) [56]
Sacrificial layer	Microphone	Kronast et al. (2001) [57]
Thin (1 micron) layer	MEMS	Dantas et al. (2008) [58]
Sacrificial layer	Microcoils	Liu et al. (2003) [59]
Nanoporous structures	Transducers	Mescheder (2004) [60]
Sacrificial layer	Microphone	Ning et al. (2004) [61]
Thick layers	MEMS	Valera et al. (2005) [62]
Patterned layer	Microneedles	Rajaraman and Henderson (2005) [63]
Sacrificial layer	Micro turbine	Rajta et al. (2009) [64]
Thin film	Microresonator	Olivares et al. (2010) [65]
Thick (15 micron) layer	Nanowire array transfer	Weisse et al. (2013) [66]
3D patterned layers	Photonic crystals	Dang et al. (2013) [67]

### 1.2.2 Porous Silicon-Based Sensing Microsystems

Mesoporous silicon is by far the most wonderful material for optical and electrical monitoring of chemical and biological molecular interactions. The integration of porous silicon transducers in microsystems is not trivial or straightforward: each step of the fabrication process (photolithography, etching, bonding/sealing, inlet/outlet) should be designed and realized, just preserving the physical and chemical characteristics of the sensing material. In case of porous silicon, pores accessibility, surface chemical features, and signal readout (both optical and electrical) should be maintained, if not optimized in microsystems fabrication.

Table 1-4 obviously depicts that this form of material has been extensively investigated as an optical sensor due to its high surface area (Fig. 1-3), high sensitivity and variety of optical transduction possibilities, e.g. changes in fluorescence or reflectance (interferometric sensing) [1].

*Table 1-4 porous silicon sensing micro systems*

<b>Transduction</b>	<b>Sensing application</b>	<b>Reference</b>
Electrical	Humidity	Rittersma et al. (2000) [68]
Electrical	Bacteria	Misra et al. (2001) [69]
Optical	Volatile compounds	De Stefano et al. (2004) [70]
Optical	Liquids/gases	De Stefano et al. (2006a) [71]
Optical	DNA	De Stefano et al. (2006b) [72]
Optical	Liquids/gases	De Stefano et al. (2006c)
Electrical	Gases	Barillaro et al. (2007)
Electrical	Gases	Zellers et al. (2007)
Optical	DNA	Rendina et al. (2007)
Optical	DNA	De Stefano et al. (2007a) [73]
Optical	Gases	De Stefano et al. (2007b) [74]
Optical	Liquids/gases	De Stefano et al. (2007c) [75]
Optical	Gases	De Stefano et al. (2007d)[76]
Mechanical	Liquids	Strambini et al. (2012) [77]
Optical	Liquids	Barillaro et al. (2012) [78]
Optical/electrical	Liquids/gases	Caliò et al. (2015) [79]

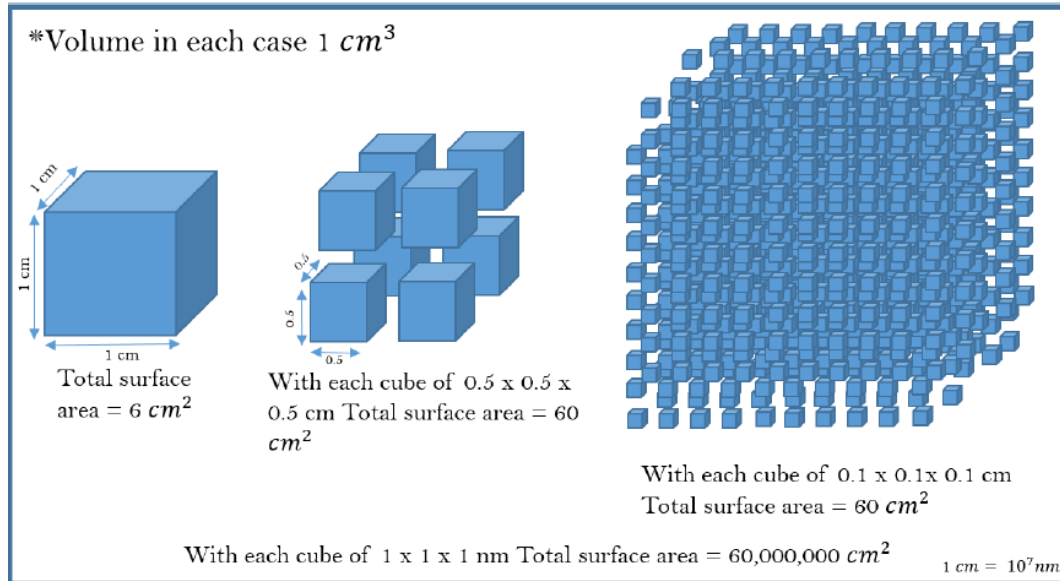


*Fig. 1-3 Surface area enhancement by miniaturization, Reprinted from Sensors and Actuators, 268, Paladya, A. Kiani, "Nano structured sensing surface: Significance in sensor fabrication", Copyright (2018) with permission from Elsevier [80]*

### 1.2.3 Porous Silicon Optical Biosensors

The rapidly developing field of porous silicon-based biosensors that utilize optical transduction is comprehensively reviewed by distinguishing the differing strategies for small- and moderate-size biomolecular analytes and the challenges with analysis of complex biofluids. A number of topics are identified for future research that should lead to one-shot disposable chip-based systems becoming commercially available.

Biosensors are analytical devices that incorporate a biological or a biomimetic recognition element (e.g., enzyme, antibody, antigen, nucleic acid, imprinted polymers, etc.) with a physiochemical transducer [81]. Thus, the major function of a biosensor is to convert the biological recognition event into a measurable and quantifiable signal [82].

Biosensors are generally classified into subgroups according to the signal transduction mode such as optical, electrochemical, and mass-sensitive measurements [81,83]. Optical biosensors offer significant advantages over both conventional analytical techniques [84] and other types of sensors for multi-target sensing and continuous monitoring [85]. Thus, these powerful detections and analysis tools have vast applications in biomedical research, healthcare, pharmaceuticals, food safety, environmental monitoring, and homeland security [85].

The application of porous Si (PSi) substrates for biosensing was first described by Thust et al. [88], demonstrating a potentiometric biosensor for the detection of penicillin. However, it is the pioneering work of Sailor and co-workers on PSi-based optical biosensors Dancil et al. 1999 [89] that has inspired the extensive research in the field [90]. Indeed, over the past decade, PSi has emerged as a promising nanomaterial for label-free optical biosensing applications as its optical properties, i.e., photoluminescence (PL) and reflectance, are highly sensitive to the presence of chemical and biological species inside the pores [91,92]. PSi offers a unique combination of versatile photonic architectures with large volume and surface area, which can be easily functionalized with a wide repertoire surface chemistry, allowing the design of sophisticated biosensing platforms (Jane et al. 2009 [93]; Bonanno and Segal 2011 [86]; Dhanekar and Jain 2013 [94]).

The optical properties of nanocrystalline silicon can be recruited to perform various therapeutic or diagnostic tasks—for example, quantum confined silicon nanostructures can act as photosensitizers to produce singlet oxygen as photodynamic therapy. A long-term goal is to harness the optical, electronic, and chemical properties of porous Si that can allow the particles to settle at diseased tissues such as tumors and then perform various tasks in vivo. These tasks include detecting, identifying, imaging, and delivering therapies to the tissue of interest. [95]

### 1.3 Highlights of Fabrication Methods

Although there exists a solid background for the application and manufacture of different forms of silicon films, there are still production techniques that can be explored for novel applications. These fascinating small dimension structures can be generated by various ways: either (Top-Down approach) reduction of the silicon crystal size, e.g. by anodic etching to form a porous surface layer (1), or by laser treatment of the surface (4), or (Bottom-Up approach) growing nanostructures, e.g. by laser crystallization of amorphous silicon (5), incorporate silicon nanoparticles inside silicon dioxide (6), deposition of superlattices (7), or deposition of nanocrystalline films by various methods [96]. Fig. 1-4 shows conventional porous silicon fabrication schematically.

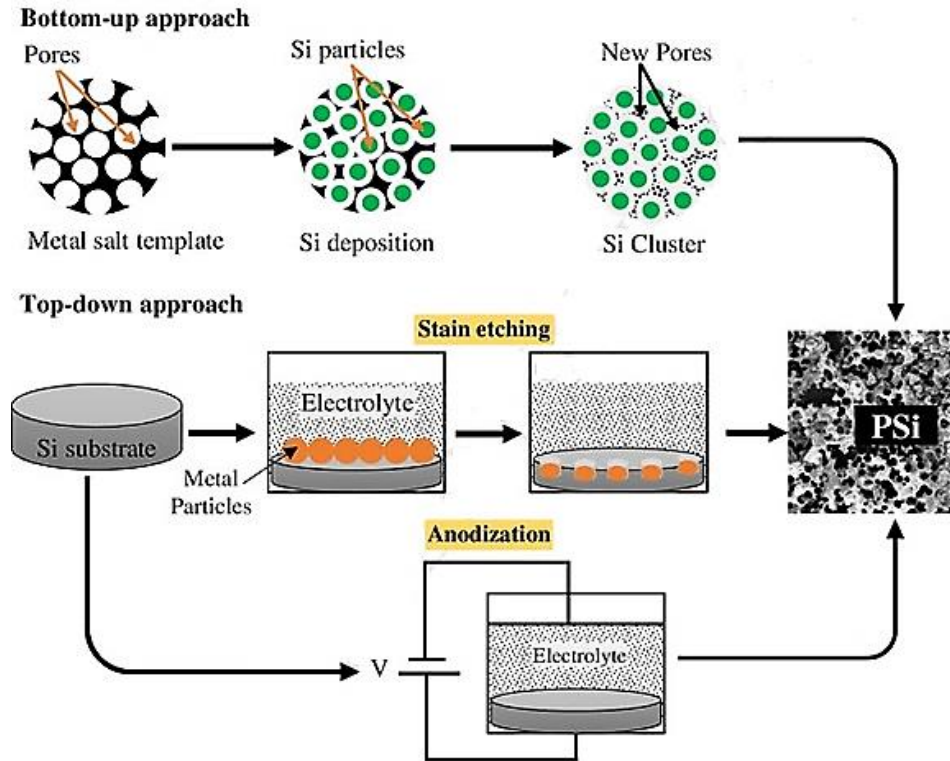


*Fig. 1-4 Schematic of porous Si synthesis by a bottom-up approach, stain etching, and anodization [97]*

Regarding top-down approach, electrochemical anodization is the most commonly used technique among them. The electrochemical etching is performed in a hydrogen fluoride (HF) solution. The etching rates are controlled by adjusting the electrolyte compositions and etching current densities. It is well known that the etching current is governed by the hole (+) generation at the Si surface to assist anodic oxidation during the electrochemical etching. In this method, two electrodes are needed. One supplies electrons to the solution (the cathode) and the other removes electrons from the solution (the anode). It is important to keep in mind that the two electrodes are required to maintain charge neutrality and to complete the electrical circuit. Regardless of the oxidation or reduction reactions occurring at the electrodes, you cannot perform electrochemistry if you do not complete the circuit. This means that at least two reactions are occurring simultaneously in an electrochemical cell, the anode (oxidation) reaction, and the cathode (reduction) reaction. Electrochemists refer to these as “half-reactions” A schematic of a two-electrode cell for etching silicon, with the relevant half-reactions, is shown in Fig. 1-5. The fabrication process of PSi

structures by electrochemical etching is a cost-competitive and versatile method, where a variety of porous structures with outstanding physical and chemical properties can be produced. This has turned porous Si into one of the most widespread materials, which is currently present in many research fields with multiple applications. This section deals with the different aspects involved in the production of macroporous Si, mesoporous Si, and microporous Si structures by electrochemical etching of silicon wafers.

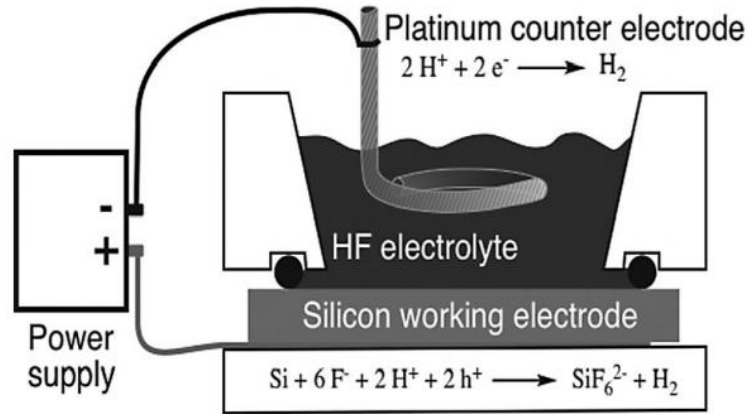


*Fig. 1-5 Schematic diagram of etching cell used for PSi formation by electrochemical etching [95]*

For p-type Si, the holes are the majority charge carriers, and the p-type PS layers are easy to produce. On the other hand, n-type PS is very difficult to form since the holes are the minority. Most of the research done on PS has been made on hole-rich p-type Si. However, the control of n-PS is necessary since an application based on n-type substrate is possible in light-emitting diode technology and microelectronic technology [95].

Recent works carried out by few research groups in the last decade (Venkatakrisnan et al.[100] and Kiani et al. [98,99]) revealed that in broad ranges of laser fabrication parameters, a fibrous nanostructure is formed due to the agglomeration of nanoparticles in the ambient atmosphere. The nanostructure formation mechanism was explained by existing theories regarding nanoparticle formation through femto/picosecond laser ablation.

Kiani and his research group [98-100] have studied the effect of laser processing parameters like power, various combinations of laser power and frequencies, scanning overloop and line spacing on patterned surface characteristics like pattern width, size of particles, the conductivity of porous nanowires, doping concentration and diameter of nanowires [101].

Laser ablation is discussed in-depth as follows. In order to remove an atom from a solid by the means of a laser pulse, one should deliver energy above the binding energy of that atom. Thus, to ablate the same amount of material with a shorter pulse one should apply higher laser intensity approximately in inverse proportion to the pulse duration. For example, laser ablation with 100fs pulses requires an intensity in the range  $\sim 10^{13} - 10^{14}$  W/cm<sup>2</sup>, while 30–100 ns pulse ablates the same material at the intensities  $\sim 10^8 - 10^9$  W/cm<sup>2</sup>. At intensities above  $10^{13} - 10^{14}$  W/cm<sup>2</sup> ionization of practically any target material takes place early in the laser pulse time. It is instructive to compare the above-defined ablation threshold to that for the long laser pulses. This also helps in considering a general picture of the ablation process in a whole range of laser pulse duration.

The ultra-short pulse laser-matter interaction mode corresponds to conditions when the electron-to-ion energy transfer time and the heat conduction time exceed significantly the pulse duration,  $\tau_{ei} \sim t_{heat} \gg t_p$  where  $t_p$  is the pulse duration [102]. Then the absorbed energy is going into the electron thermal energy, and the ions remain cold, making the conventional thermal expansion inhibited. However, as shown above, if the laser intensity is high enough, the electrons can gain energy in excess of the Fermi energy and escape from the target. The electromagnetic field of the charge separation created by the escaped electrons pulls the ions out of the target. Hence, the extreme nonequilibrium regime of material ablation takes place. This regime occurs at the laser pulse duration  $t_p < 200$  fs and at the intensities above  $10^{13} - 10^{14}$  W/cm<sup>2</sup>. The escaped electrons accelerate the ions by the electrostatic field of charge separation [102].

An intermediate regime takes place at the laser pulse duration  $0.5\text{ps} < t_p < 100\text{ps}$  and at the intensities less than  $10^{11}$  W/cm<sup>2</sup>, when  $\tau_{ei} \sim t_{heat} \sim t_p$  and  $T_e \sim T_i$  (electron and lattice equilibrium). The most appropriate description of the heating and expansion processes in this regime is given by the conventional two-temperature approach. At the longer laser pulse duration  $t_p > 10\text{ps}$  the heat conduction and hydrodynamic motion dominate the ablation process,  $t_p \gg \tau_{ei}, t_{heat}$ . The electrons and the lattice are in equilibrium early at the beginning of the laser pulse  $T_e \sim T_i$ . Hence, the limiting case of thermal expansion (thermal ablation) is suitable for the description of the long pulse ablation mode [102]. The difference in the ablation mechanisms for the thermal long-pulse regime and the nonequilibrium short pulse mode is two-fold.

First, the laser energy absorption mechanisms are different. The intensity for the long pulse interaction is in the range  $10^8$ –  $10^9$  W/cm<sup>2</sup> with the pulse duration change from nanoseconds to picoseconds. The ionization is negligible, and the dielectrics are almost transparent up to the UV range. The absorption is weak, and it occurs due to the interband transitions, defects, and excitations. At the opposite limit of the femtosecond laser-matter interaction, the intensity is in excess of  $10^{13}$  W/cm<sup>2</sup> and any dielectric is almost fully ionized in the interaction zone. Therefore, the absorption due to the inverse Bremsstrahlung and the resonance absorption mechanisms on free carriers dominate the interaction, and the absorption coefficient amounts to several tens' percent [96, 102].

Second, the electron-to-lattice energy exchange time in a long pulse ablation mode is of several orders of magnitude shorter than the pulse duration. For this reason, the electrons and ions are in equilibrium, and ablation has a conventional character of thermal expansion. By contrast, for the short pulse interaction the electron-to-ion energy exchange time, as well as the heat conduction time, is much larger than the pulse duration, and the ions remain cold. Electrons can gain energy from the laser field in excess of the Fermi energy and escape the target. The electric field of a charge separation pulls ions out of the target thus creating an efficient nonequilibrium mechanism of ablation [102].

Post-processing operations such as heat-treatments are employed for the study or advancement of thin-film performances [103, 104]. Treatments may affect different thermal rate regimes or vacuum/specific atmosphere conditions [105]. Due to application conditions and possible harsh influences caused by working temperature on the thin film, it seems to be an essential research area to study the effects of high temperature on optical behavior. As of the amount, microstructural, compositional, and morphological changes may occur in the nanostructure. The recrystallization process accompanied by the nature of the structure and topography may result in a robust, resilient, or shaky attitude to temperature variation.

In the following chapters the selective optical properties of a group of thin films synthesized by pulsed laser fabrication technique are studied. Samples are tested as-deposited and heat-treated for their response in transmission and reflection.

## Chapter 2.

### Experiments and Techniques

#### 2.1 Materials and Overview

The ultrashort laser material removal mechanism in the transition range of pico- and nanosecond pulse durations has raised debates in the last decade and it is still theoretically far from well known. Four determining factors mean power (P), frequency (Frq) or repetition rate, pulse duration (Pd), and scanning speed (SS), are varied to generate groups of samples. Thin films are synthesized by irradiating a laser beam onto an n-type  $\langle 100 \rangle$  (manufactured using Czochralski process — one side polished) orientation silicon wafer which was placed approximately a quarter of a millimeter from a glass slide. Both the silicon wafer and the glass slide substrate were held parallel in a vertical position. Experiments were conducted by using the raw material from crystalline silicon wafers  $\langle 100 \rangle$  (ALPHA Malaysia) and conventional microscope slides.

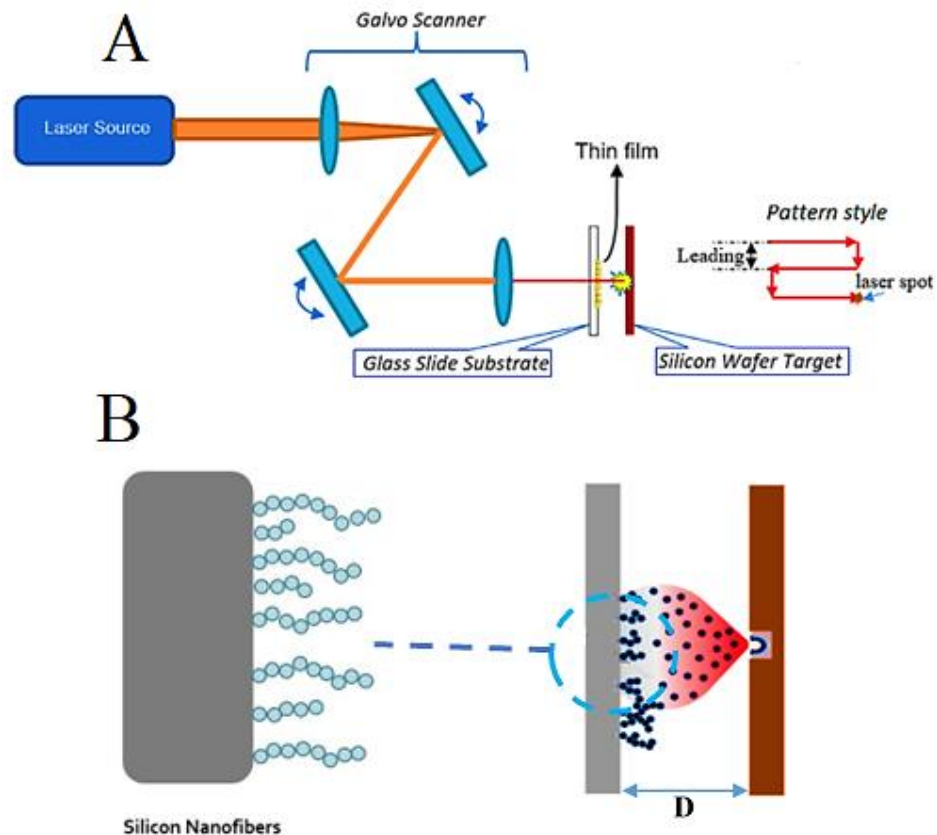


Fig. 2-1 Schematic A) experiment set-up B) nanostructure formation [120]

A picosecond Ytterbium pulsed laser (IPG Germany) was employed as a beam source. Films were generated, while air-exposed, in square shapes (nearly  $8 \times 8$  mm) in order to maintain an acceptable focus of the laser galvo scanner. A schematic of our experimental arrangement is shown in Fig. 2-1. A fiber laser source produced a beam of 1064 nm wavelength that was directed into a galvo scanner, pre-programmed to inscribe a pattern on the silicon target. Meanwhile, the laser-induced plasma led to partial nano-fiber deposition on a glass substrate. The characteristics of these films were probed and are described in the following sections. Film generation parameters are presented in Table 2-1 with their description.

*Table 2-1 Thin films manufacturing factors [120]*

<b>Parameter</b>	<b>Type</b>	<b>Range</b>
Frequency	<i>variable</i>	<i>600-1200 kHz</i>
Power	<i>variable</i>	<i>6.5-15 W</i>
Pulse duration	<i>variable</i>	<i>150 ps-5 ns</i>
Speed	<i>variable</i>	<i>10-100 mm/s</i>
Pitch (leading)	<i>constant</i>	<i>0.025 mm</i>

2.2 Tools and Equipment

Thin films were produced by a Ytterbium pulsed fiber laser (IPG Laser Model: YLPP-1-150V-30) with a 1064 nm wavelength. The laser diameter of 7.6 mm was reduced to 6 mm using an iris diaphragm which was then focused toward an XY galvanometer scanner (JD2208 by Sino-Galvo). Employing an F-theta lens with a focal length of 63.5 mm, input aperture of 14 mm, and a beam displacement of 18.7 mm, the scanner provided a theoretical laser spot diameter of 20  $\mu$ m. The interfacing software used to set patterning parameters was MarkingMate 2.7. Kiani’s lab is equipped with a pulsed laser setup illustrated in Fig. 2-2.

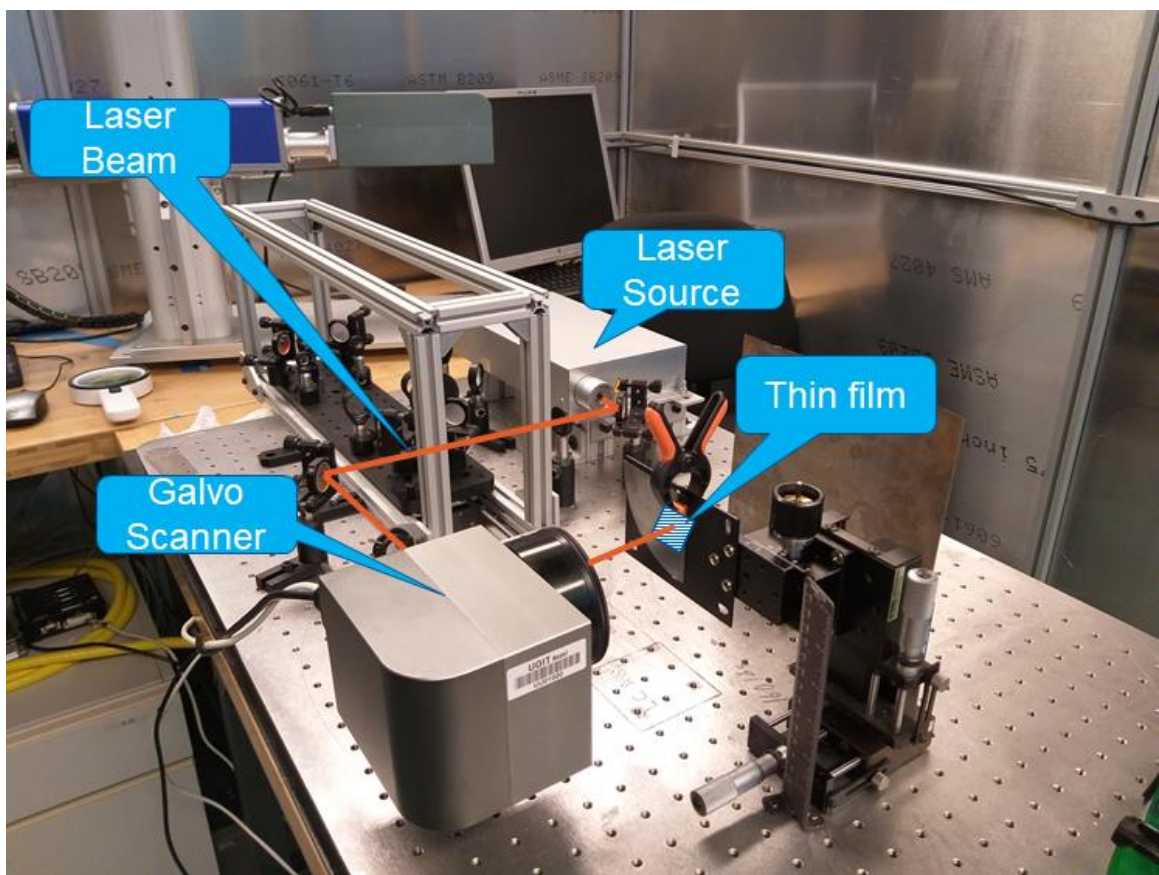


*Fig. 2-2 Pulsed laser setup with components and their arrangement*

FTIR (PerkinElmer Spectrum 100), utilized to characterize the constituents qualitatively. Raman spectroscopy (Renishaw Raman Imaging Microscope System 2000) was used to identify the functional groups and to compare the high-intensity peaks quantitatively. SEM (FEI Quanta 3D 200/600) and light spectroscopy (Ocean Optics UV-Vis USB2000+ & STS-NIR) were used to study topographical and structural features as well as reflection and transmission spectra in UV-Vis and NIR range, respectively. Source light was provided by Fiber-Lite MI-150. XRD measurements were carried out for crystalline analysis with a Rigaku MiniFlex 600 diffractometer (Bragg-Brentano geometry) equipped with a NaI scintillation counter detector and a monochromatized Cu K $\alpha$  radiation source ( $\lambda = 1.5406 \text{ \AA}$ ) operating at a voltage of 40 kV and current of 15 mA. Compositional study was done by XPS measurements, a Thermo Scientific K-alpha XPS system. An Al K $\alpha$  source with a 400  $\mu\text{m}$  spot size was used to determine the presence of specific elements.

### 2.3 Characterization techniques

*SEM (Scanning Electron Microscopy)*: In general, a scanning electron microscope (SEM) can make images of solid samples so that it reveals information on topography and surface morphology [106]. The low end of the magnification range for an SEM is typically on the order of 20X to 50X. The maximum magnification is generally determined by the size of the electron beam and can be as high as one million ( $10^6$ ). These magnification levels generally correspond to measuring features from the mm scale down to nm size. The best resolution of a high-end SEM is on the order of 0.5 nm. The most common type of SEM data is the secondary electron image. The SE image is a map of secondary electron emission as a function of spatial position. Backscattered electrons (BSE) are the second most common imaging data collected with an SEM. This data is a map of backscattered electron emission as a function of spatial position. In addition to collecting imaging data to show the morphology of a sample, SEMs also generate and can collect X-rays that are characteristic of the elements in the sample. This is usually done with an energy dispersive X-ray spectrometer or EDS system. EDS X-ray data can be used to determine the elements in the sample. Essential components of all SEMs include the following (Fig. 2-3):

- Electron Source ("Gun")
- Electron Lenses
- Sample Stage
- Detectors for all signals of interest
- Display / Data output devices
- Infrastructure Requirements:
  - Power Supply
  - Vacuum System
  - Cooling system
  - Vibration-free floor
  - Room free of ambient magnetic and electric fields

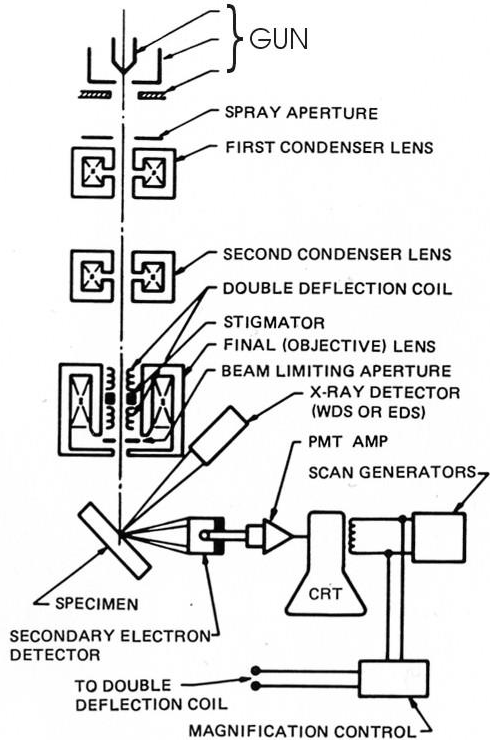
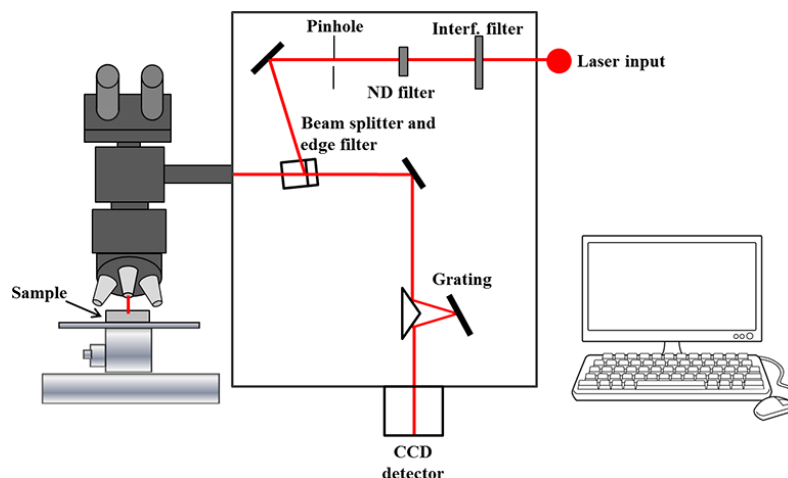


Fig. 2-3 Schematic drawing of an SEM instrumentation [107]

*Raman Scattering Spectroscopy:* A form of molecular spectroscopy based on the Raman effect, described above. A laser beam is used to irradiate a spot on the sample under investigation. The scattered radiation produced by the Raman effect contains information about the energies of molecular vibrations and rotations, and these depend on the particular atoms or ions that comprise the molecule, the chemical bonds connect them, the symmetry of their molecule structure, and the physio-chemical environment where they reside.

From the identities of minerals, we know the chemical formulas and the arrangements of the atoms within them. Thus, we know whether the mineral was a carbonate, sulfate, phosphate, silicate, oxide, sulfide, hydroxide, etc. In some cases for which chemical compositions can vary, e.g., in the ratio of iron to magnesium ions, we can determine the cation ratio [108].

The basic equipment configuration consists of a light source for irradiating the sample with light, a spectrometer that disperses the scattered light, and a detector that detects the scattered light (Fig. 2-4). Besides, with a microscopic Raman spectrometer, by combining a microscope, it is possible to extract information in a minute area of less than 1  $\mu\text{m}$ [109].



*Fig. 2-4 Raman scattering spectroscopy facility [108]*

*FTIR (Fourier Transform Infra-red Spectroscopy):* When IR radiation is passed through a sample, some radiation is absorbed by the sample, and some passes through (is transmitted). The resulting signal at the detector is a spectrum representing a molecular ‘fingerprint’ of the sample [110]. The usefulness of infrared spectroscopy arises because different chemical structures (molecules) produce different spectral fingerprints. So,

- The Fourier Transform converts the detector output to an interpretable spectrum
- The FTIR generates spectra with patterns that provide structural insights

The FTIR spectrometer uses an interferometer to modulate the wavelength from a broadband infrared source. A detector measures the intensity of transmitted or reflected light as a function of its wavelength [111]. The signal obtained from the detector is an interferogram, which must be analyzed with a computer using Fourier transforms to obtain a single-beam infrared spectrum (Fig. 2-5). The FTIR spectra are usually presented as plots of intensity versus wavenumber (in  $\text{cm}^{-1}$ ). Wavenumber is the reciprocal of the wavelength. The intensity can be plotted as the percentage of light transmittance or absorbance at each wavenumber [112].

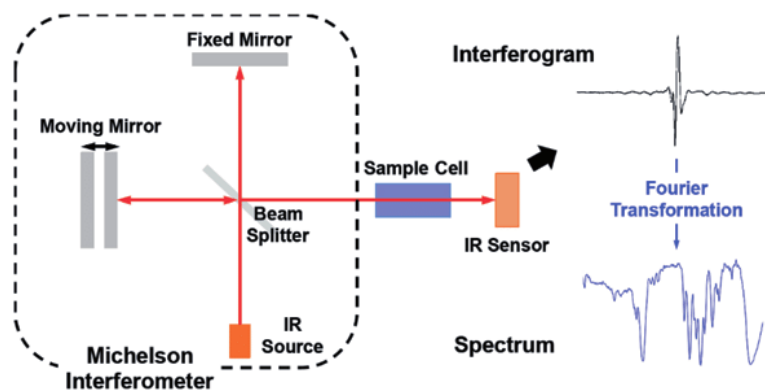


Fig. 2-5 FTIR spectroscopy generic schematic [110]

*XPS (X-ray Photoelectron Microscopy)*: This is an analytical technique where x-rays are used to bombard a specimen and the energies of emitted electrons are analyzed. Typical x-ray sources are  $MgK\alpha$  at 1253.6 eV and  $AlK\alpha$  at 1486.6 eV. Analysis with an ultraviolet source at 21.2 eV can also be made to provide high count rates for the low energy region which contains valence band information [113]. X-rays penetrate the specimen surface to a depth of a few micrometers but only the electrons near the surface can be emitted without losing energy due to collisions with other atoms [114]. The kinetic energy (KE) of the electrons is measured and the binding energy (BE) of the electrons can be determined with a simple relationship:

$$h\nu = KE + BE + \phi \quad (2-1)$$

where  $h\nu$  is the x-ray energy and  $\phi$  is the spectrometer work function (usually only a few eV). An energy spectrum is obtained with a scan over the kinetic energy range from 0 eV to the incident x-ray energy. The energy spectrum is different for each element and permits elemental identification of the species present in the top 1-2 nm. The detection limit is approximately 0.1% atomic. XPS is more sensitive to higher atomic number elements [115].

An XPS apparatus substantially consists of a high-vacuum environment, a source of fixed energy radiation, an electron energy analyzer coupled with a lens system to disperse the emitted electrons according to their kinetic energy, an electron detector to measure the flux of emitted electrons of a particular energy, and a flood gun for charge compensation [116]. Typically, the apparatus is then connected to a computer with a proper software interface, which registers the signal coming from the detector, and a spectrum of counts rate vs kinetic

energy will be displayed in real-time. After the acquisition, data processing tools are generally provided to extract all the required information. Fig. 2-6 depicts a block diagram of a typical XPS spectrometer.

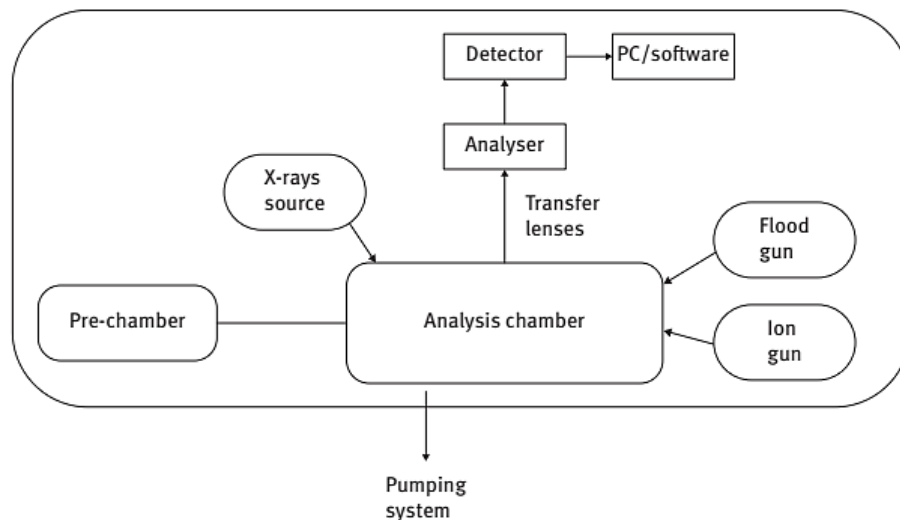


Fig. 2-6 Schematic diagram of an XPS spectrometer [107]

*XRD (X-ray diffraction)*: This method is one of the most important characterization tools used in solid-state chemistry and materials science, which could provide the most definitive structural information (e.g. interatomic distances, bond angles, crystallinity, etc...)[117]. The extensive use of X-rays for the analysis of atomic structural arrangements is based on the fact that the wavelength of the X-ray is in the  $1 \times 10^{-10}$ m range, which is the same order magnitude of the atomic spacings in crystalline solids. When x-rays interact with the crystal lattice, a simple model called Bragg's law can be used to understand the required conditions for diffraction. Bragg's law can be expressed as [117]:

$$n\lambda = 2d\sin\theta \quad (2-2)$$

where  $\lambda$  is the wavelength of X-ray,  $d$  is the spacing between layers of an atom,  $\theta$  is the angle between incident X-ray beam and scattering plane, and  $n$  is an integer (Fig. 2-7).

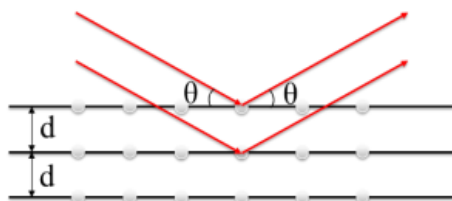
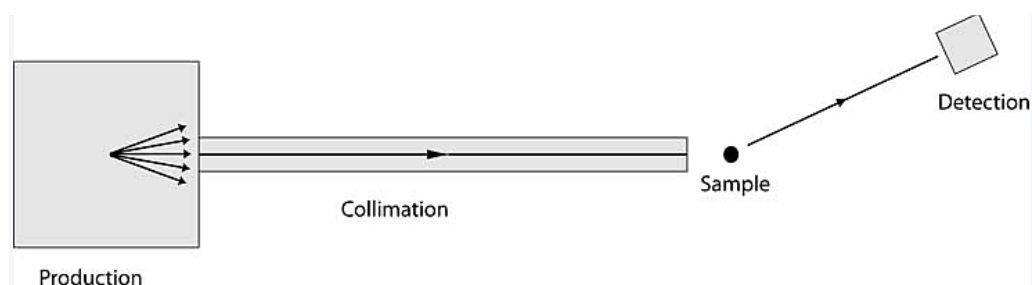


Fig. 2-7 a generic X-ray scattering measurement

Thus, the diffracted waves will consist of sharp interference maxima (peaks) with the same symmetry as in the distribution of atoms if the atoms are arranged in a periodic fashion in crystals. And the structural information of the crystals can be revealed based on the diffraction peaks [118, 119].

Although there are many possible permutations, essentially all XRD instruments incorporate the components shown in the following schematic: a means of producing the x-ray radiation, some kind of collimation, something to support the sample (and possibly orient it or maintain the desired environment), and a means for detecting the scattered radiation (Fig. 2-8)[117].



*Fig. 2-8 Schematic of an XRD basic components*

#### 2.4 Statistical analysis

Several measures have been taken to identify and diminish sources of error in designing the experiments and collecting data. Entire laser set-up alignments were checked before each and every experiment. The focal point of the laser beam was obtained by the same procedure of adjustment for each run. The gap between the slide glasses and silicon wafers were set precisely constant to ensure unvarying conditions. Optics laboratory apparatus, holders, and clamps were secured to stand sturdy and without any clearances. Data acquisition devices as light spectroscopies were calibrated per manufacturer's procedures and the light source was left 30 minutes idle on before test commencement to avoid any drift over time. Three samples were synthesized for each set of manufacturing parameters and spectral measurements were done three times for each sample. The series with the minimum variance and less than 5% Euclidean distance at any point was selected as the final spectrum for further considerations.

## Chapter 3.

### 1<sup>st</sup> Study: Laser nanofabrication parameter study<sup>1</sup>

#### 3.1 Introduction

During the past decade, there has been great interest in the versatility and simplicity of the pulsed laser technique to deposit thin films on a substrate. Controllable nanofabrication parameters, along with a wide range of material alternatives, have enabled researchers to find ways to control nano-scale structures in thin film generation. Silicon and its derivatives like SiO<sub>2</sub> are essential materials for industrial applications such as semiconductors, optoelectronics, and telecommunication. Nano-structured silicon films that consist of 1D fibrous elements were previously proven to be a group of pulsed laser products. They provide an amazingly large contact surface area, which is porous and highly useful for sensing technology. Among various characteristics of interest in thin film study, optical properties continue to be the main focus of research due to the ease of measurement and interpretation. Thin film generation variables can be governed to meet an optical criterion. This approach paves the way to scalable and reproducible nano-manufacturing [120].

#### 3.2 Sample preparation

Thirty six samples were prepared with fabrication parameters as per following Table 3-1 Quantity and manufacturing variables:

*Table 3-1 Quantity and manufacturing variable [120]*

Parameter	Value	Parameter	Value	Parameter	Value	Parameter	Value
Power	6.5 w	Frequency	600 kHz	Pulse Duration	150 ps	Scanning Speed	10 mm/s
	10 w		900 kHz		1 ns		100 mm/s
	15 w		1200 kHz		5 ns		200 mm/s

<sup>1</sup> Chapter 3 has been published with title ‘Optical properties of Si/SiO<sub>2</sub> nano structured films induced by laser plasma ionization deposition’ in Optics Communication, <https://doi.org/10.1016/j.optcom.2020.125297>

### 3.3 Results and Discussion

The variations in laser parameters listed in Table 3-1 Quantity and manufacturing variable could potentially change the nature of manufacturing process from a pure thermalization to non-thermal ablation or a combination. A thorough experimental assessment of the correlation between deposition parameters and material properties would help us understand the pure theoretical complexities and obtain a better grasp of the most relevant options for developing functional groups of thin films. In this study, the basic optical features of the samples were obtained and compared to one another.

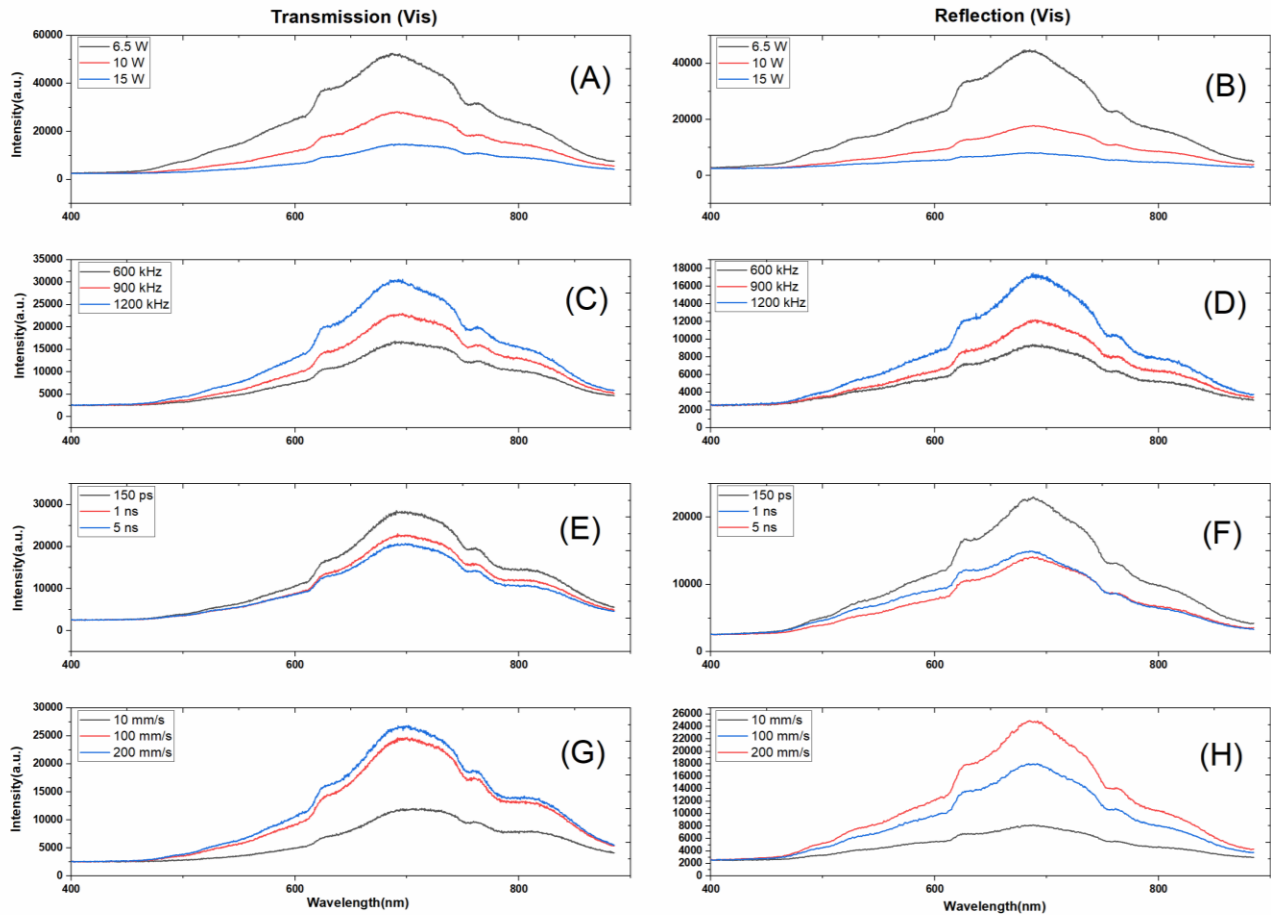


Fig. 3-1 Vis range transmission (A, C, E, G) and reflection (B, D, F, H)[120]

Fig. 3-1 shows Vis range transmission and reflection spectra of the films recorded over 3 values for each variable P, Frq, Pd, and SS. NIR spectra for transmission and reflection for the same variables are represented in Fig. 3-2.

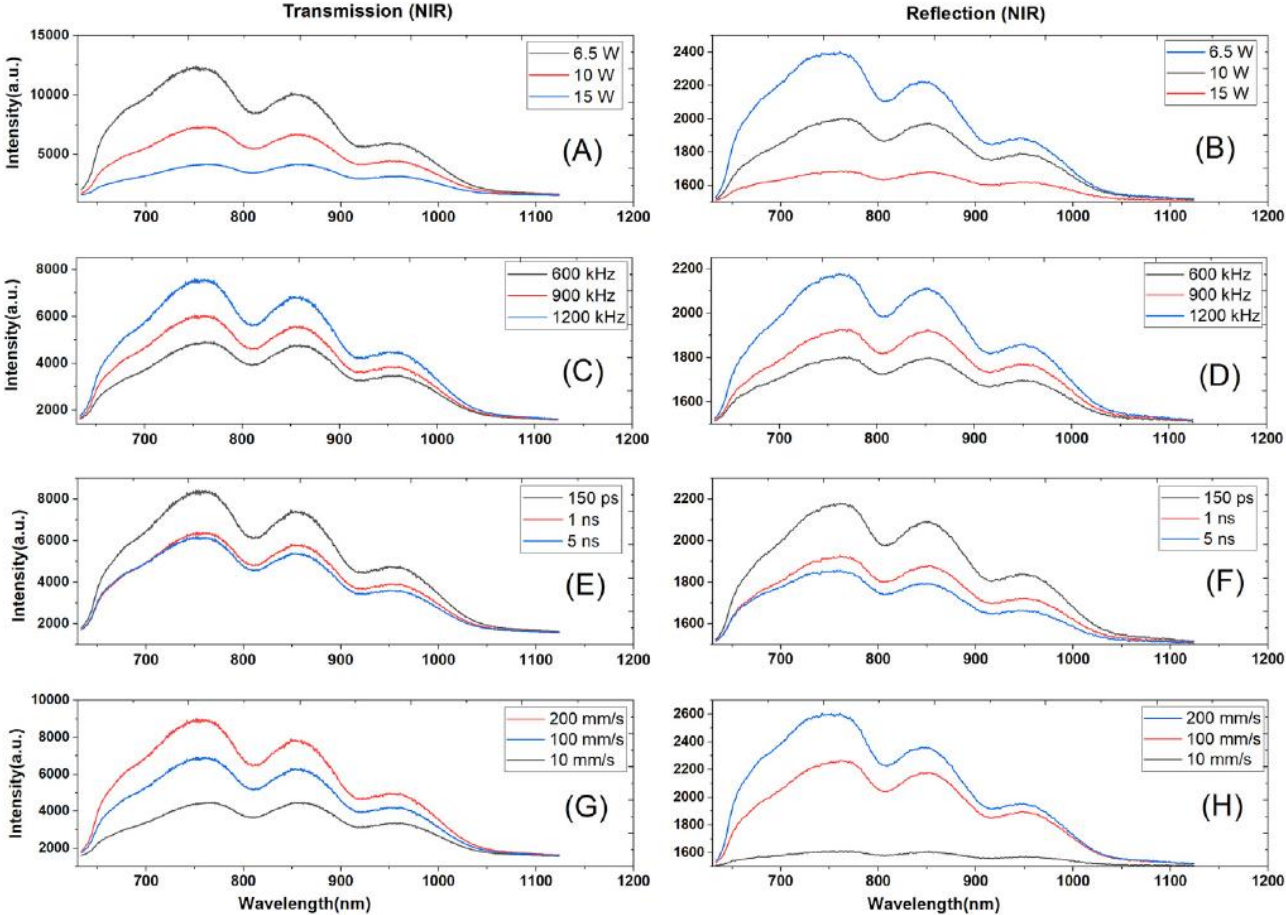


Fig. 3-2 NIR range transmission (A,C,E,G) and reflection (B,D,F,H) [120]

Table 3-2 shows the trends in illustrated Fig. 3-1 and Fig. 3-2 to assist the reader in comprehension. By and large, ordinate intensities are all either directly or reversely proportional to change in variables.

A bare glass slide was used as reference for data collection. Since there was a large gap between the reference intensities, we have presented all above generated graphs normalized along with the corresponding references. Normalization is performed based on the maximum value of each set of data.

Table 3-2 Trends in Fig. 3-1, Fig. 3-2 [120]

Variable Increase		Vis spectra Intensity	NIR spectra intensity
<i>Power</i>	<i>P1=6.5 W</i>	<i>Decrease</i>	<i>Decrease</i>
	<i>P2=10 W</i>		
	<i>P3=15 W</i>		
<i>Frequency</i>	<i>Frq1=600 kHz</i>	<i>Increase</i>	<i>Increase</i>
	<i>Frq2=900 kHz</i>		
	<i>Frq3=1200 kHz</i>		
<i>Pulse duration</i>	<i>Pd1=150 ps</i>	<i>Decrease</i>	<i>Decrease</i>
	<i>Pd2=1 ns</i>		
	<i>Pd3=5 ns</i>		
<i>Scanning speed</i>	<i>SS1=10 mm/s</i>	<i>Increase</i>	<i>Increase</i>
	<i>SS2=100 mm/s</i>		
	<i>SS3=200 mm/s</i>		

Figures 3-3 and 3-4 show the normalized diagrams in the Vis and NIR ranges of the precursors. They are another functional tool for deriving latent qualities to compare and judge the logged data from a new perspective.

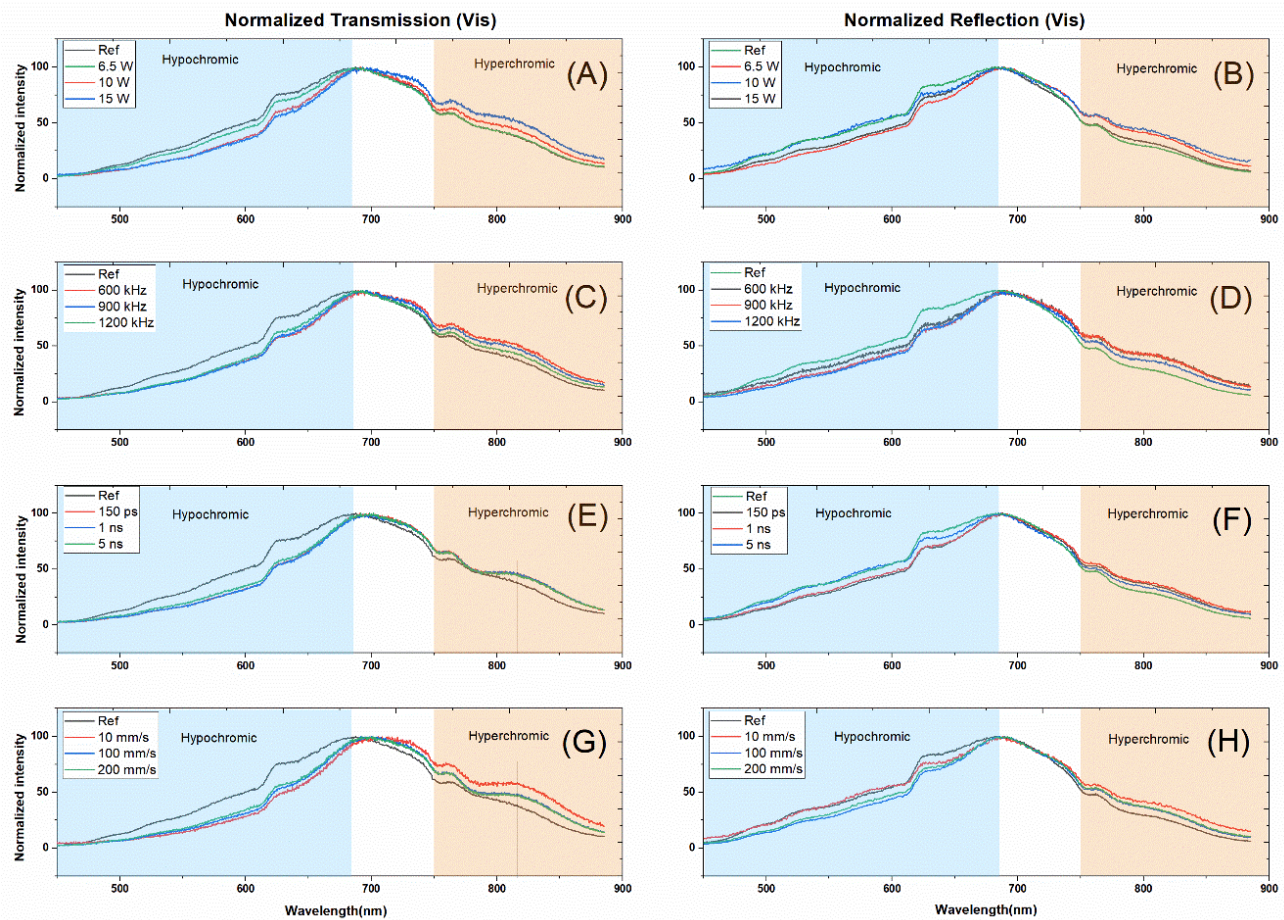


*Fig. 3-3 Vis range transmission (A,C,E,G) and reflection (B,D,F,H) normalized graph [120]*

Normalized graphs are useful in spotting notable shifts to lateral or vertical directions. In general, all the optical spectroscopy results shown in Fig. 3-3 exhibits hypochromic behavior below 690 nm and hyperchromic above 750 nm (specified with shaded areas respectively). In addition, two humps can be seen in sample spectra at 815 nm for varying scanning speed and pulse duration (Fig. 3-3 E & G), which are designated by a vertical line. No significant red or blue shift is seen in sideways orientation regarding this figure.

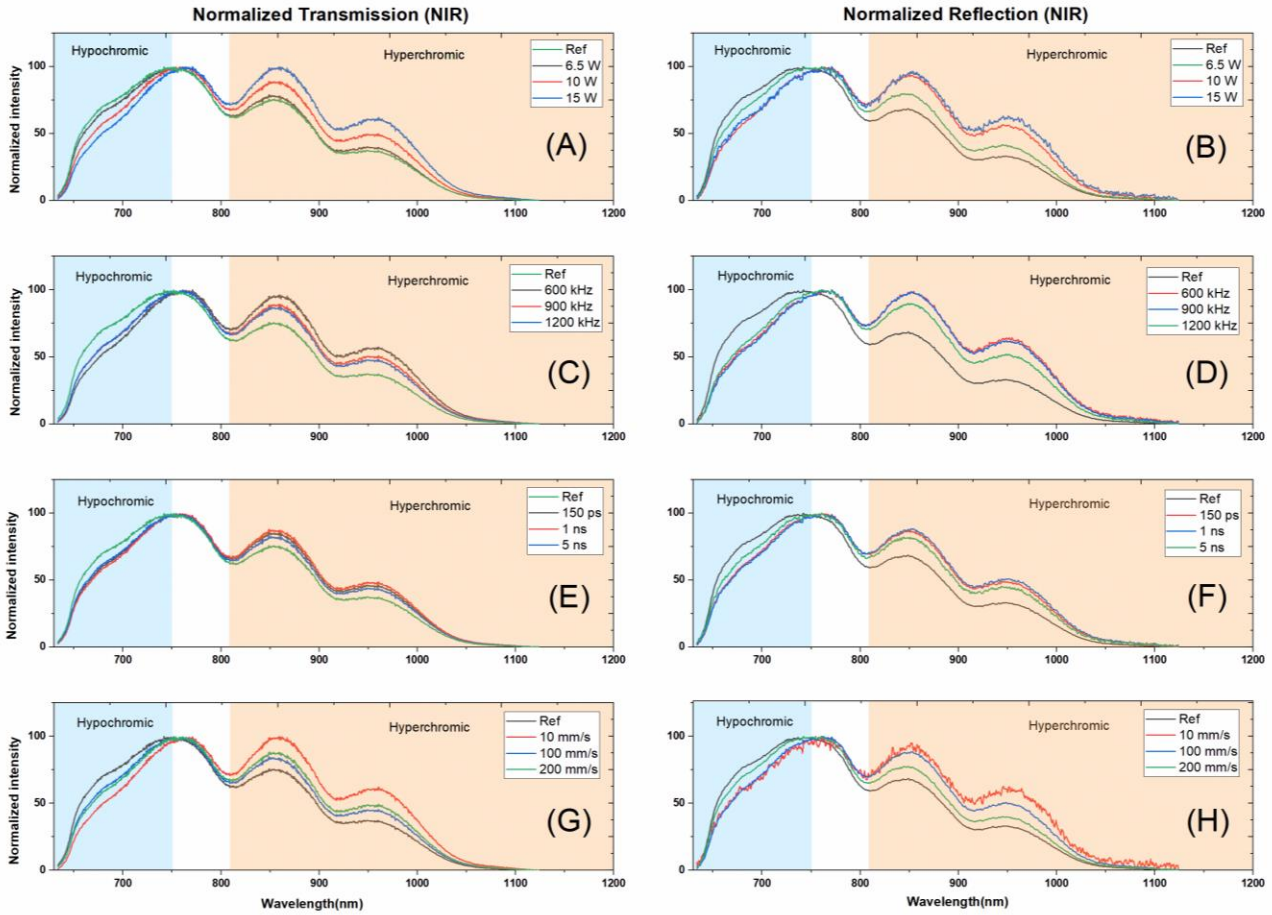


*Fig. 3-4 NIR range transmission (A,C,E,G) and reflection (B,D,F,H) normalized graph [120]*

Plotted sample data in Fig. 3-4 show a slight incremental red-shift (20 nm maximum), with reference to the substrate normalized Ref spectrum. Over the domain range of variables, a hypochromic and hyperchromic response is evident for under 750 nm and above 810 nm respectively (color-shaded areas in Fig. 3-4).

SEM images, shown in Fig. 3-5, based on sample numbers, were used to verify structural and geometrical features of the settled layers. The uniform surface topology can be witnessed for P3, Frq3, Pd2, Pd3, SS2, and SS3 samples. Uniform and evenly distributed fibrous structures are apparently observed with power and frequency increases, while for justification of pulse duration and scanning speed variation samples, these should be considered together with material characteristics outcomes. SEM images were also utilized to measure fiber diameters using ImageJ v1.52a software for 30 randomly chosen points of each sample [121]. The trend for fiber diameters was consistent with power peak variation

(Table 3-3, 3-4) except for speed, which does not affect the power peak. Excluding the Frq1 sample, which has no fibrous structure, diameters ranged from 40 to 250 nm. Different proportions in each sample show a similar standard deviation (~18 nm) for each sample measurement. Most of the samples show particulates of 350 to 500 nm diameter tangled in threadlike morphology.

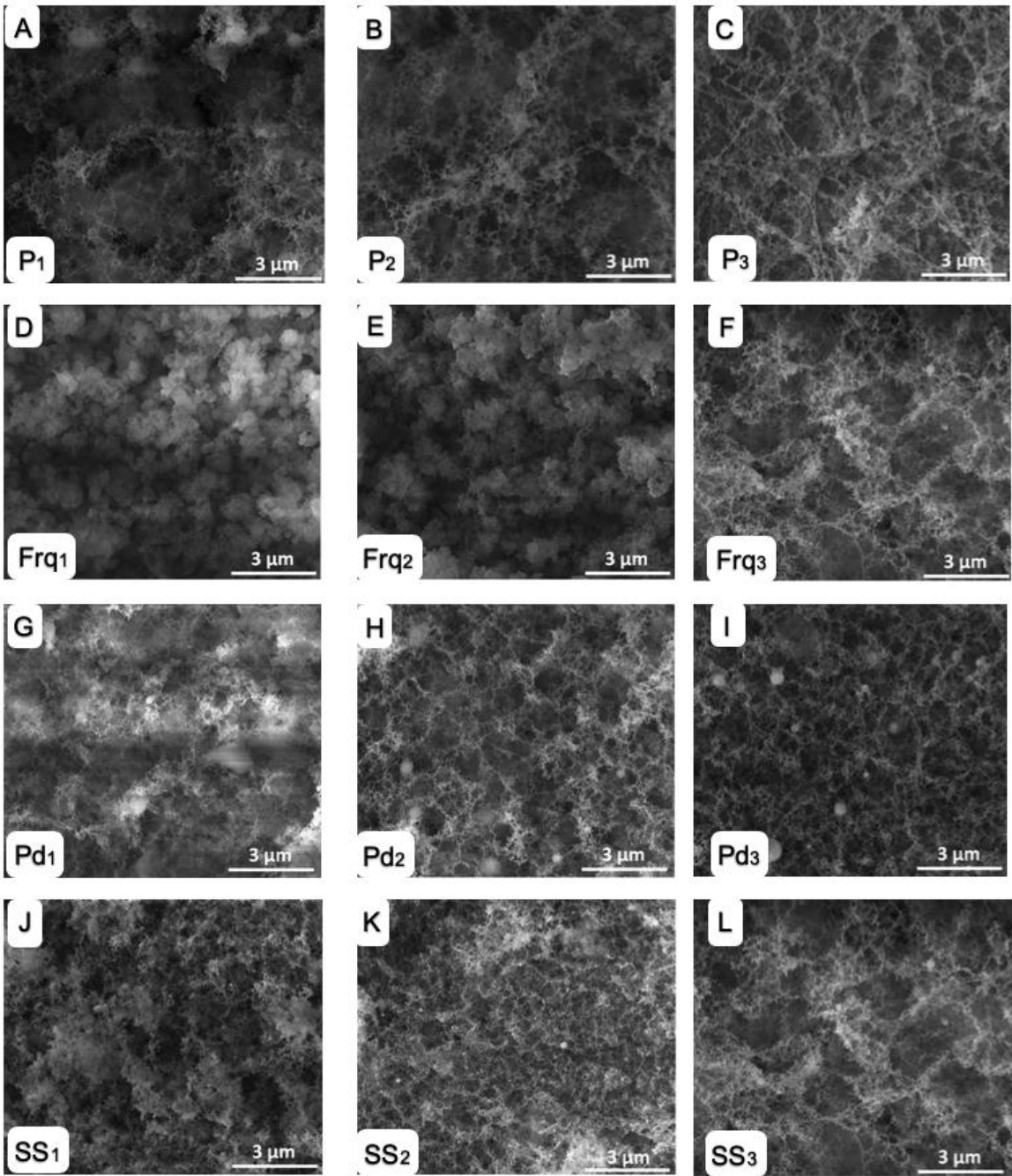


*Fig. 3-5 SEM images magnified at X20K of samples in four groups: (A,B,C) for power, (D,E,F) for frequency, (G,H,I) for pulse duration and (J,K,L) for speed changes [120]*

The average surface temperature also greatly affected the thermalization regime on the target and solidified the crystalline anatomy of the ablated particles on the substrate [122-124]. This is shown in Figure 3-6 based on the effective number of pulses.  $N_{eff}$  is calculated by substituting the radius of the laser spot,  $\omega_o$  ( $\approx 15\mu\text{m}$ ), the velocity  $v$  and the frequency  $f$  into the equation:

$$N_{eff} = \sqrt{\pi/2} \omega_o f / v . \quad (3-1)$$

The following are the equations used to obtain an estimate of the average surface temperature on the substrate. The average surface temperature can be calculated using the equation [122, 123]:

$$T_{avg}(n) = 2\alpha \frac{\left[\left(1 - \frac{2}{3}\right)\alpha\right]}{(1 + \alpha^2)} \frac{T_m}{(1 - \alpha)} \left[1 + \frac{\alpha^n - \alpha}{n(1 - \alpha)}\right] \quad (3-2)$$

In which  $n$  is the effective number of pulses.  $T_m$  in the equation is the maximum surface temperature at the end of a single pulse, determined by [14][123]:

$$T_m = \sqrt{\frac{2a}{\pi^3 t_p} \frac{4K(1 - R)P}{k f d^2}} \quad (3-3)$$

Where the thermal diffusion coefficient,  $a$ , is  $8.5 \times 10^{-5} \text{m}^2/\text{s}$ . The thermal conductivity,  $k$ , is  $155 \text{ W/mK}$ . The laser spot diameter,  $d$ , is  $30 \times 10^{-6} \text{ m}$ . The reflection coefficient,  $R$ , is  $0.325$ . The residual energy coefficient,  $K$ , is  $0.8$ , and the power of the laser,  $P$ , is kept at  $10 \text{ W}$ . Lastly, the pulse duration,  $t_p$ , is  $150 \text{ ps}$  for all cases.

The constant ratio for the previous maximum and the following minimum temperatures,  $\alpha$ , is calculated by:

$$\alpha = \sqrt{\frac{t_p}{t_{pp}}} \quad (3-4)$$

where  $t_{pp}$  is the pulse interval and is simply the inverse of the frequency, as shown by:

$$t_{pp} = \frac{1}{f} \quad (3-5)$$

The theoretical results of the dependence of average surface temperature on the pulse numbers, across manufacturing parameter changes, are illustrated in Fig. 3-6.

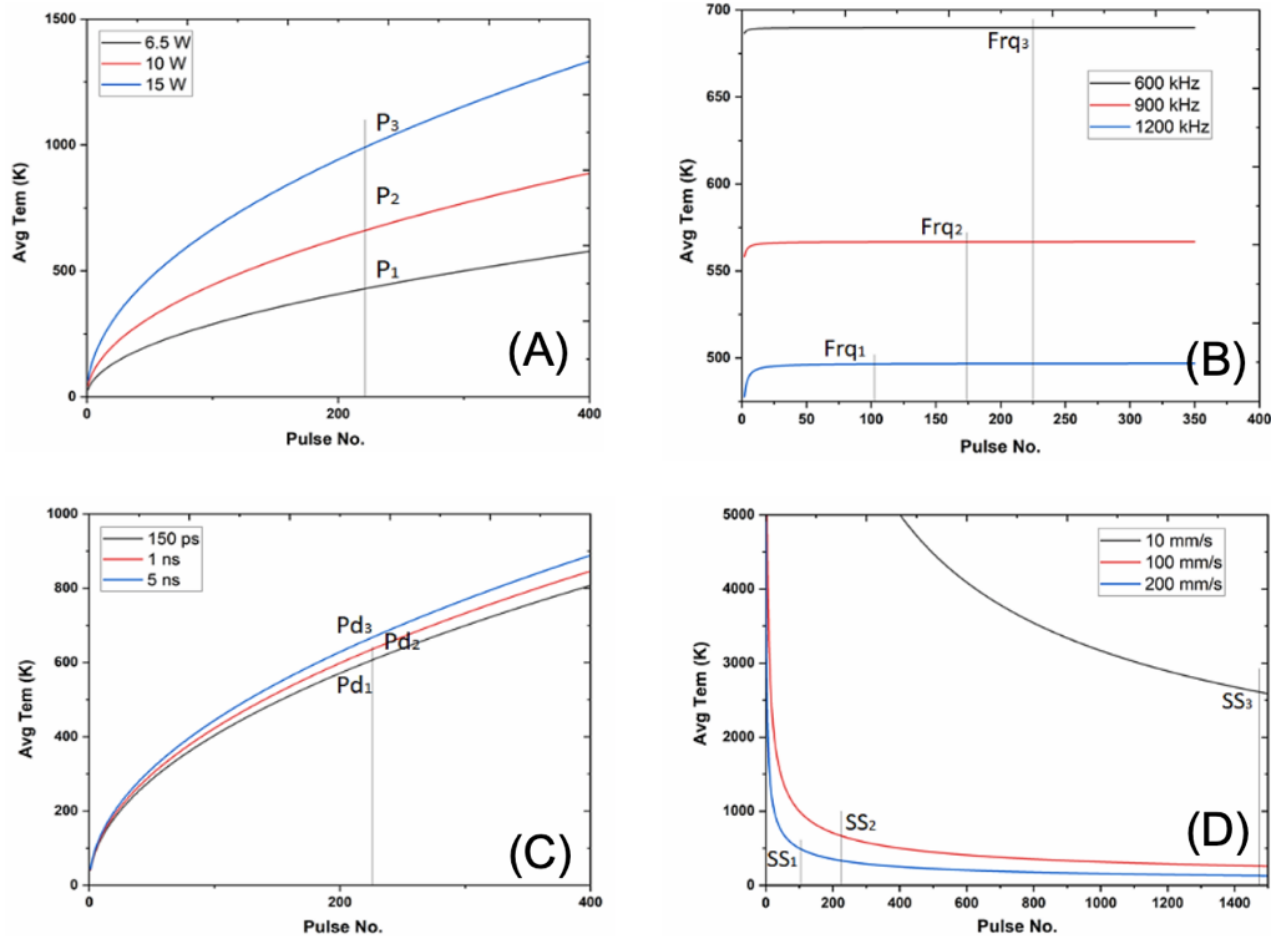


Fig. 3-6 Average surface temperature of the target surface with P, Frq, Pd and SS samples against effective pulse numbers [120]

Thickness measurements were done with moderate accuracy using an optical microscope camera from multiple points randomly chosen on the film. The rate of error was about 10%.

Table 3-3 Average film thickness [120]

	Avg film thickness in $\mu\text{m} \pm 10\%$ error		
<b>Power (P<sub>1</sub>,P<sub>2</sub>,P<sub>3</sub>)</b>	13.2	16.5	26.4
<b>Frequency (Frq<sub>1</sub>,Frq<sub>2</sub>,Frq<sub>3</sub>)</b>	23	16.5	16.5
<b>Pulse duration (Pd<sub>1</sub>,Pd<sub>2</sub>,Pd<sub>3</sub>)</b>	19.8	16.5	23
<b>Scanning speed (SS<sub>1</sub>,SS<sub>2</sub>,SS<sub>3</sub>)</b>	46.2	26.4	23

A last useful criterion is the peak power,  $P_{\text{peak}} = P_{\text{avg}} / (f \cdot \tau)$ , where  $f$  stands for frequency and  $\tau$  is the pulse duration. It is a measure of surface excitation potential that should be combined with the properly chosen value for its constituents to optimize ablation and film quality

(Table 3-3 Average film thickness) [124, 125]. Notably, the peak power is not a function of scanning speed and cannot be singly revealing in this regard [123].

Table 3-4 Peak power with parameter change [120]

	Power Peak		
Power (P1,P2,P3)	3.61E4	5.56E4	8.33E4
Frequency (Frq1,Frq2,Frq3)	1.11E5	7.41E4	5.56E4
Pulse duration (Pd1,Pd2,Pd3)	5.56E4	8.33E3	1.67E3
Scanning speed (SS1,SS2,SS3)	5.56E4	5.56E4	5.56E4

Material characterization data is shown in Raman and FTIR plots (Fig. 3-7 and Fig. 3-8).

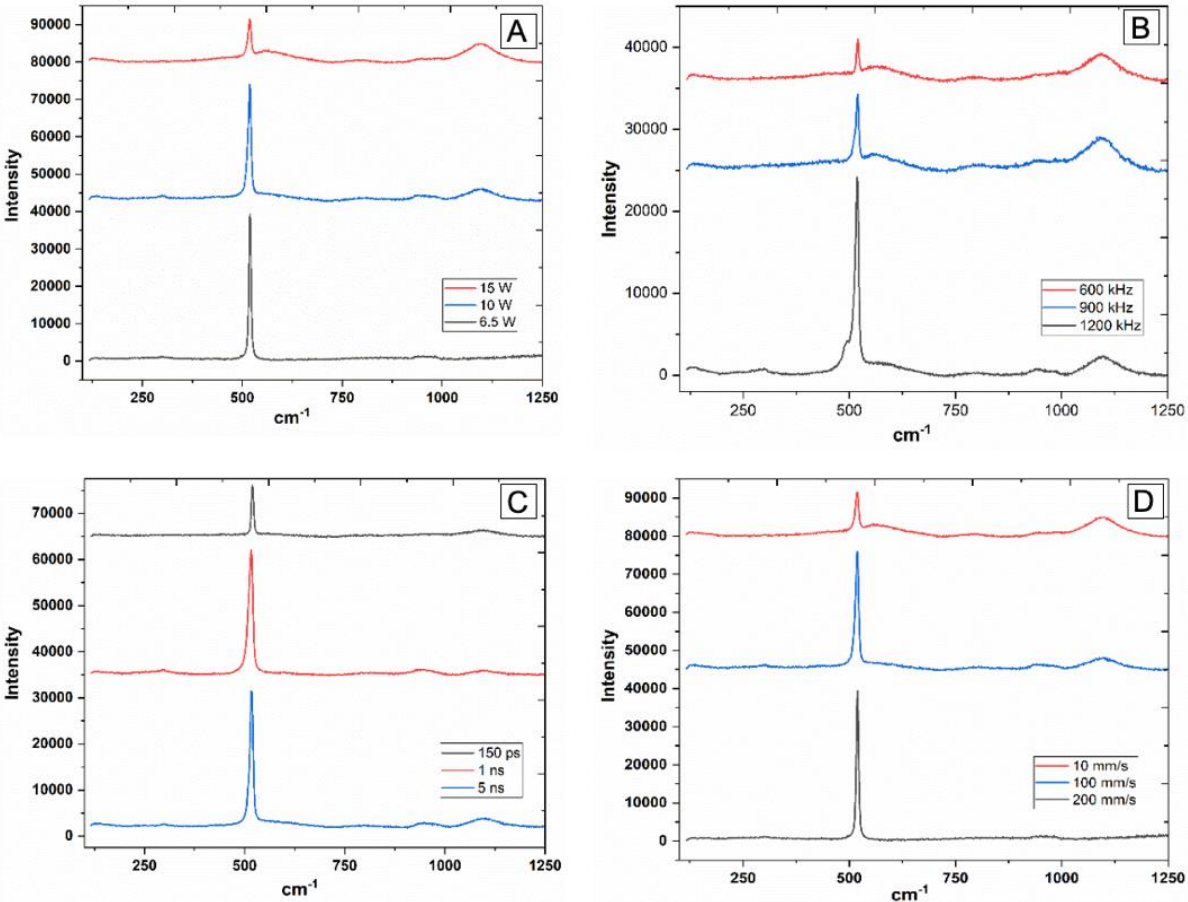


Fig. 3-7 Raman scattering spectra for groups of (A)P,(B)Frq,(C)Pd and (D)SS [120]

Average power increases (P<sub>1</sub>-P<sub>3</sub> samples) bring about high-energy pulses, which are a driving force for material removal and plume pressure [80, 125]. In this manner, more ablated mass from the target is expected to be deposited on the glass slide substrate and correspond with the film thickness (Table 3-3). This adds more obstruction in front of transmitted light in the Vis and NIR range. The porous fibrous structures are evidently becoming denser with the power rise shown in SEM images (Fig. 3-5 A,B,C), which may assist light trapping and diffuse reflection to reduce reflection intensity. On the other side, the theoretical average surface temperature that exceeds the oxidation temperature (1000 to 1300 K) with power would give rise to oxidation and SiO<sub>2</sub> content (Fig. 3-6), which is a stronger absorber compared to c-Si and varying the crystalline structure of the original silicon [126]. This agrees with Raman and FTIR data. Raman spectral features associated with c-Si and a-Si (480 to 520 cm<sup>-1</sup>) and SiO<sub>2</sub> (980 to 1200 cm<sup>-1</sup>) were observed (Fig. 3-7 A). The SiO<sub>2</sub> amount rises as the power increases, while the c-Si content lowers in associated graphs. In FTIR diagram, the transmission reduction band in 1040 to 1150 cm<sup>-1</sup> range is assigned to the stretching vibration mode of Si-O and shows an increase with power rise [127, 128]. Additionally, normalized graphs show a red shift with P<sub>3</sub> mostly on the far-right side and more distinct plots for UV-Vis spectra (Fig. 3-3 and Fig. 3-4).

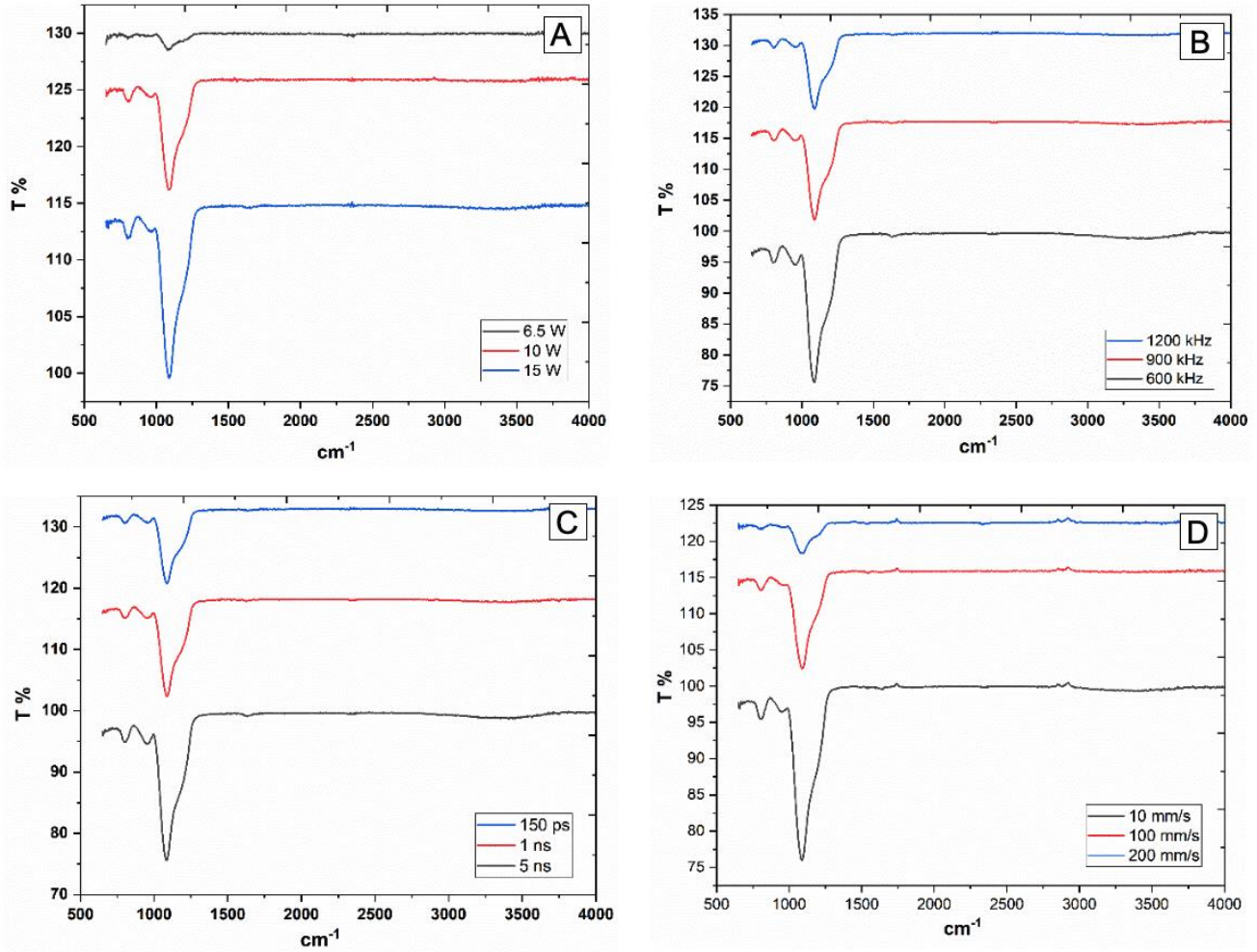


Fig. 3-8 FTIR spectra for groups of (A)P, (B)F[125]rq, (C)Pd and (D)SS [120]

As of Table 3-4 an increase in frequency (Frq1-Frq3 samples) will reduce the peak power and at the same time, the regime of material removal seems to be totally different than for other variable changes. This would lead to a significant improvement in the quality of a fine nano-fibrous structure by drastically reducing the number of evaporated atoms [125, 127]. So, the ejection of solid material clumps will be eliminated [102]. SEM images (Figure 3-5 D, E, F) confirm the hypothesis by showing large agglomerated particulates in the Frq1 sample. However, the Frq1 sample is much thicker than the other two samples (Table 3). This might be attributed to the highest peak power value among all the samples and the corresponding shock wave. That would help expel bulky molten material out the drilled hole. By increasing the frequency (Frq2 and Frq3), film thickness alone would not be a reliable method to describe the phenomenon. But the ablation mechanism, plume

distribution, and resolidification formation can play a dominant role in this regard. The difference between maximum and average temperature would be smaller with the frequency increase. This provides a more uniform substrate condition for fibrous structure generation far from the temperature shock. Raman and FTIR observations (Fig. 3-7 B, Fig. 3-8 B) over frequency decline, illustrate lower concentration but sharper and less amorphous silicon. Frq1 Raman at silicon peak shows an amorphous bump ( $\sim 480 \text{ cm}^{-1}$ ) that agrees with low-intensity transmission and reflection. The same sample also shows a higher  $\text{SiO}_2$  content, which is in line with the previous discussion. The  $\text{SiO}_2$  level is almost similar for the Frq2 and Frq3 samples, which corresponds with the FTIR results. Additionally, the theoretical results presented in Fig. 3-6 shows the average surface temperature decreasing as the frequency increases.

An increase in pulse duration (Pd1-Pd3 sample) weakens the optical intensity, but the structure is still fibrous for all the values as shown in the SEM images (Figure 6 G, H, I). Therefore the film thickness alone is misleading in analyzing pulse duration effect on optical ratings (Table 3-3) since its variation greatly affects the nature and rate of the evaporation in the process. Maximum surface temperature by the end of the pulse ( $T_{max} \propto t_p^{-\frac{1}{2}}$ ) drops with average value increase over pulse duration growth. So higher quality, non-thermal ablation with homogeneously sized fibers in Pd1 can be attributed to this. Raman scattering (Figure 3-8 C) also shows an increase in a-Si and p-Si content, which deteriorates optical properties with longer pulse durations. Although high  $\text{SiO}_2$  content is apparent in the Pd3 sample, it can be better identified by studying the FTIR spectra (Figure 3-9 C).

By varying the scanning speed (SS1-SS3 samples), we observe a great gap in the SS1 optical measurements with respect to the other two samples. This may be predominantly attributed to a marked speed drop, which leads to higher intensity and pulse numbers hitting a point. Large off-trend film thickness demonstrates this fact in SS1 predominantly (Table 3-3). Our experience shows that a lower speed ( $< 10 \text{ mm/s}$ ) would result in a bulky particulate structure rather than a fibrous nano-structured formation. Indeed, due to the lack of thickness difference, we have to compare and discuss the SS2 and SS3 samples. Silicon dioxide ( $\text{SiO}_2$ ) concentration obviously drops with scanning speed increase, as depicted in Raman and FTIR spectra (Fig. 3-7, Fig. 3-8 D). Regarding normalized graphs, apart from the first half

of the dome in the reflection spectra, we can notice a right shift in other plots with the SS1 sample standing far right.

### 3.4 Conclusion

Looking at the whole experiment comprehensively suggests that manageable thin film production for customized applications with required optical values can be achieved. Piecing together the features of different spectra would enable the implementation of simultaneous changes to the variables at hand in order to achieve an arbitrarily tuned thin porous film. Amazingly fast film generation capabilities might be tabulated and utilized for at least a rough estimate of manufacturing factors toward a specific goal.

In brief, power and pulse duration variation reversely affect the optical intensities in Vis and NIR range while frequency and scanning changes in direct order would affect the intensities of optical spectra.

## Chapter 4.

### 2<sup>nd</sup> Study: Post heat treatment of Si/SiO<sub>2</sub> thin films<sup>2</sup>

#### 4.1 Introduction

Post treatment may have either improving or degrading effect on thin films as per their application. Rough operating conditions as high temperatures and thermal stresses and the effect entail studying the post-treatment effect on samples. For example, the electrical conductivity of sputtered SnO<sub>2</sub> films was improved by an annealing process that reduced the internal stress and increased the length of the free electron mean free paths [103].

#### 4.2 Sample Preparation

A simplified schematic diagram of the fabrication set-up is shown in Fig. 4-1. Two sets of samples were pulsed laser-induced with settings listed in Table 4-1. Previous results reported by our research team show the structure and surface morphology changes with pulsed-laser parameter variation [120, 129]. Prepared samples were heat-treated, and ramp rates, holding times and cooling rates for the two groups are presented in Table 4-2.

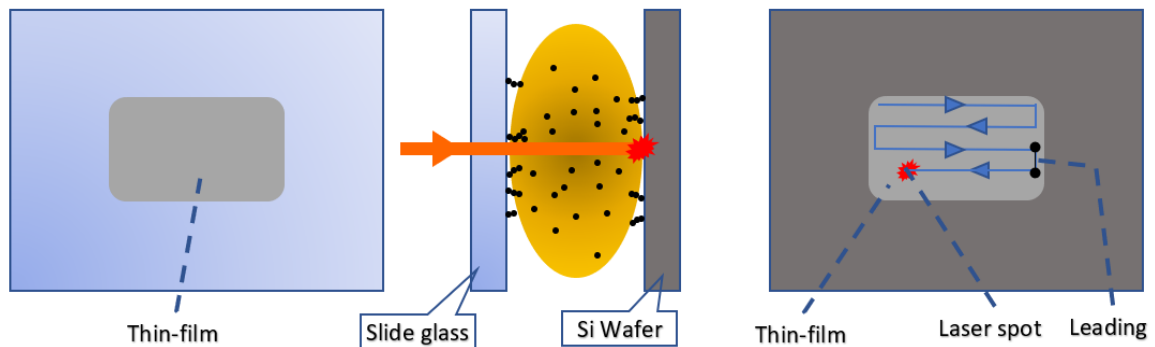


*Fig. 4-1 Schematic experiment set-up (not to scale)*

---

<sup>2</sup> The results have been submitted to the Thin Solid Film journal (figures will appear in that paper)

*Table 4-1 Manufacturing parameters*

<b>Parameter</b>	<b>Range</b>
Frequency	600, 1200 kHz
Power	10.5 W
Pulse duration	150 ps
Scanning speed	100 mm/s
Pitch	0.025 mm

*Table 4-2 Produced samples*

<b>Group No.</b>	<b>Mfg. Parameter</b>	<b>Heat treatment</b>
1	Freq. : 600 kHz	S11 room temp.
		S12 400°C
		S13 1000°C
2	Freq. : 1200 kHz	S21 room temp.
		S22 400°C
		S23 1000°C

#### 4.3 Results and Discussion

The laser ablation of silicon is caused by both thermal and non-thermal procedures [130]. Key parameters such as pulse energy, repetition rate, and target material characteristics govern the nature of ablation. High energy per pulse with low frequency and amplified silicon absorption led to a thermal for Group1: S11, S12, S13, while lower pulse energy and high repetition contributed to a more non-thermal atom removal, as in Group2: S21, S22, S23. The former created a 3D rough structure comprised of deposited droplets, while the latter made nano-fibrous structures that were highly porous. SEM images verified the effect of frequency change in pulsed laser material removal. Typical SEM images with low and high magnification scales are shown for group1 (Fig. 4-2 C, D) and group2 (Fig. 4-2 A, B) samples.

The reflection spectra  $R(\lambda)$ , Fig. 4-3 A, B, of the thin films were measured in the visible wavelength range (400 to 900 nm) and were thereafter background deducted. Heat-treated samples at 400°C and 1000°C were respectively the most and the least reflective in the domain. Untreated reflection spectra were located somewhere in the middle. Reflection curves gradually merged by moving from the mid-zone to either NIR and UV extremes.

Fig. 4-4 depicts the reflectance (R%) versus wavelength with reference to the reflection spectrum of the clean bare glass substrate. Although the above-mentioned arrangement and order repeat themselves here, slope and steepness differ over wavelength. Fig. 4-3 and Fig. 4-4 prove the robustness and stable optical response of porous structures (S21 to S23) to post-production annealing as opposed to the high variation in particulate structure (S11 to S13), which is aligned with our previous work [131, 132]. Originally, a reduced reflection intensity in the as-deposited (S11, S21) sample of group1 relative to its counterpart in group2 is attributed to a bulky amorphous structure and less SiO<sub>2</sub> content [120].

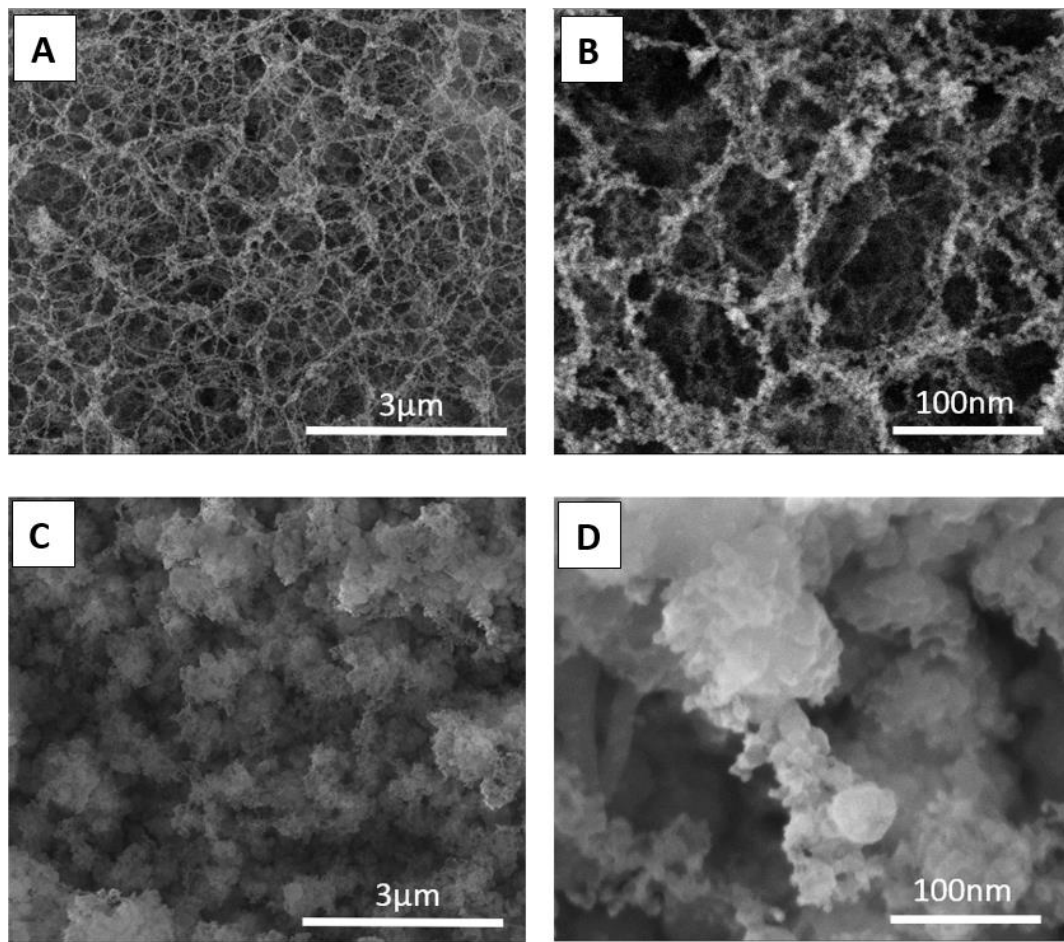


*Fig. 4-2 Typical SEM images of two groups of samples with low and high magnification (A,B typically show S11 to S13 and C,D, typically shows S21 to S23)*

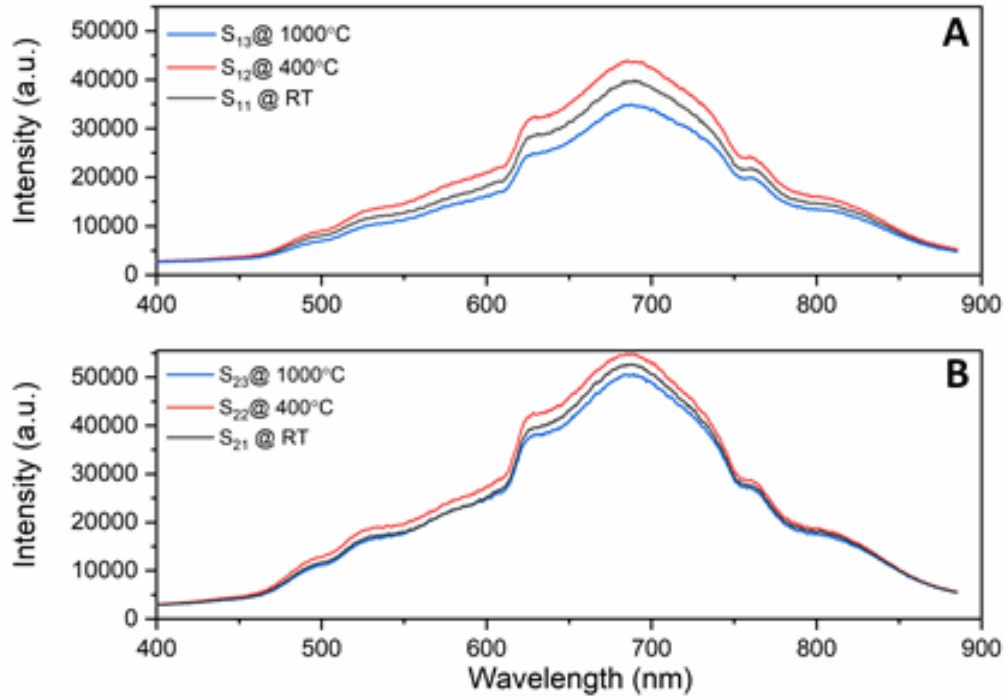


Fig. 4-3 Vis range reflection spectrum for two sets of samples (A: Group1, B: Group2)

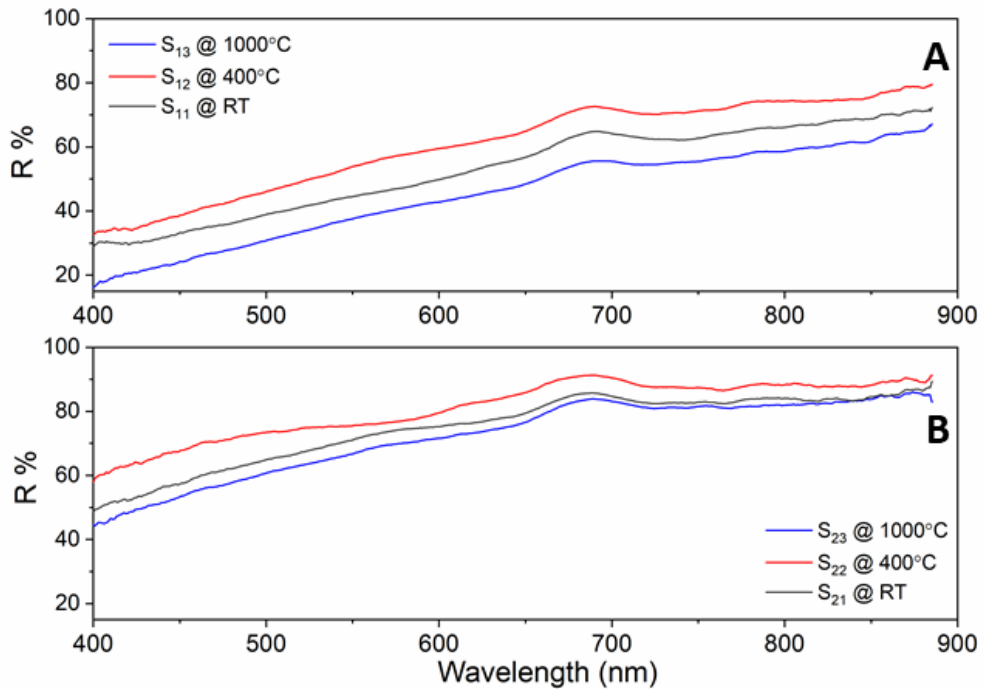


Fig. 4-4 Vis range reflectivity of two groups of samples (A:600kHz, B:1200kHz) with heat treatment

XPS Spectral distribution in Fig. 4-5 and Fig. 4-6 present peak intensities for silicon (Si 2s, Si 2p), carbon (C 1s), and oxygen (O 1s) and Auger oxygen. The Si 2s and Si 2p peaks, at

~153 eV and ~103 eV respectively, O 1s at ~532.5 eV, C 1s at ~284.5 and Auger O at ~980 eV. Si and O peaks are incomparable to others and will be analyzed further. Relative concentration of carbon is very small and can be explained by ambient contamination that occurs in most air-stored samples [133]. As can be observed, both Si and O peaks increase by the set temperature of post-treatment (Fig. 4-5 and Fig. 4-6 A, C, E and Figure 7). They are connected with Si-O bonding mainly in SiO<sub>2</sub> (Fig. 4-5 and Fig. 4-6 B, D, F). Additionally, the gap between the peak intensities is higher for group1 samples than for group2 samples. This gap in Fig. 4-7 correlates with the variation of reflectance from the as-deposited samples for each of these groups in Fig. 4-3. A large gap can be seen between S11 with heated S12, S13 while the smaller difference is seen between group2 samples, S21 with S22 and S23 (Fig. 4-3).

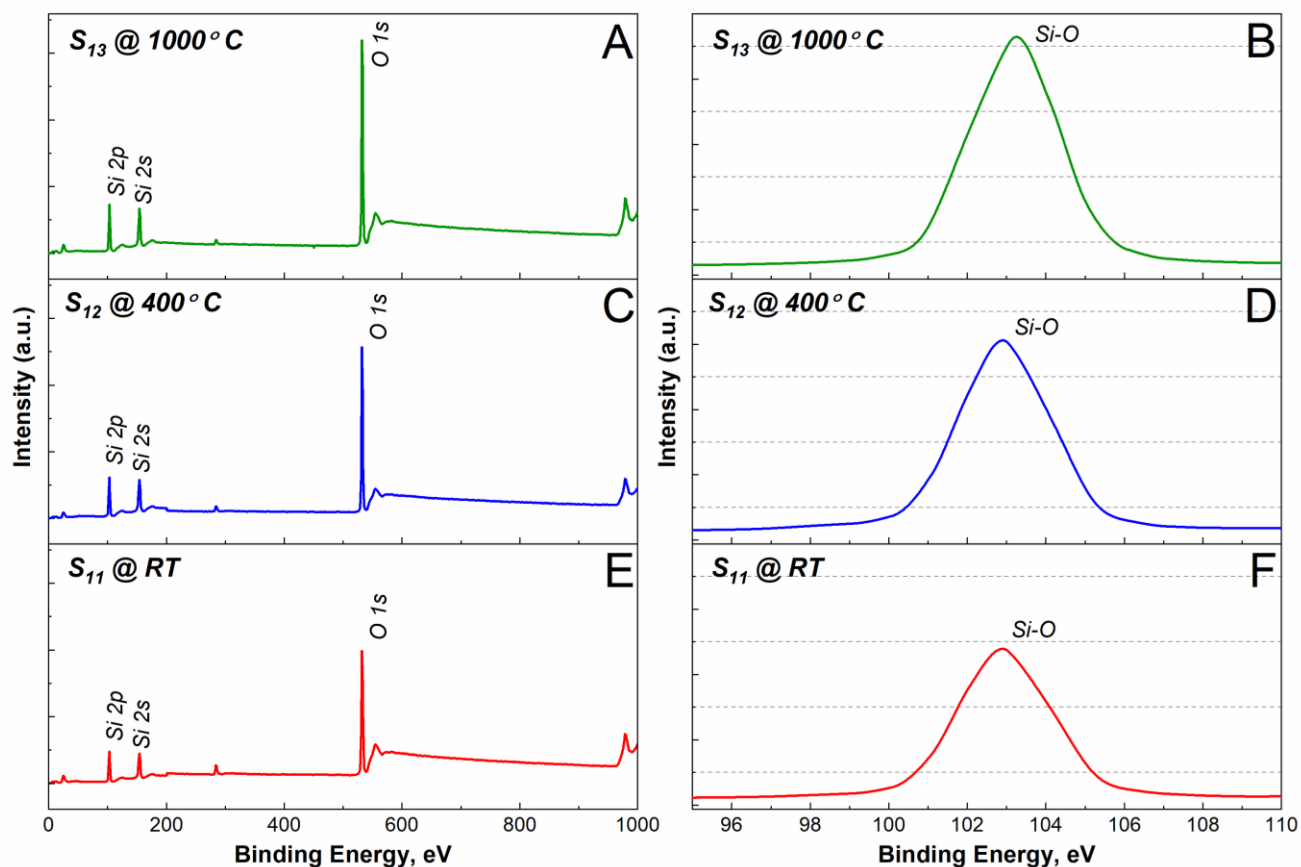


Fig. 4-5 XPS survey spectra of group1 samples, 600kHz, (A,C,E) and XPS narrow cut spectra and chemical state analysis for the Si 2p region at ~103 eV, (B,D,F)

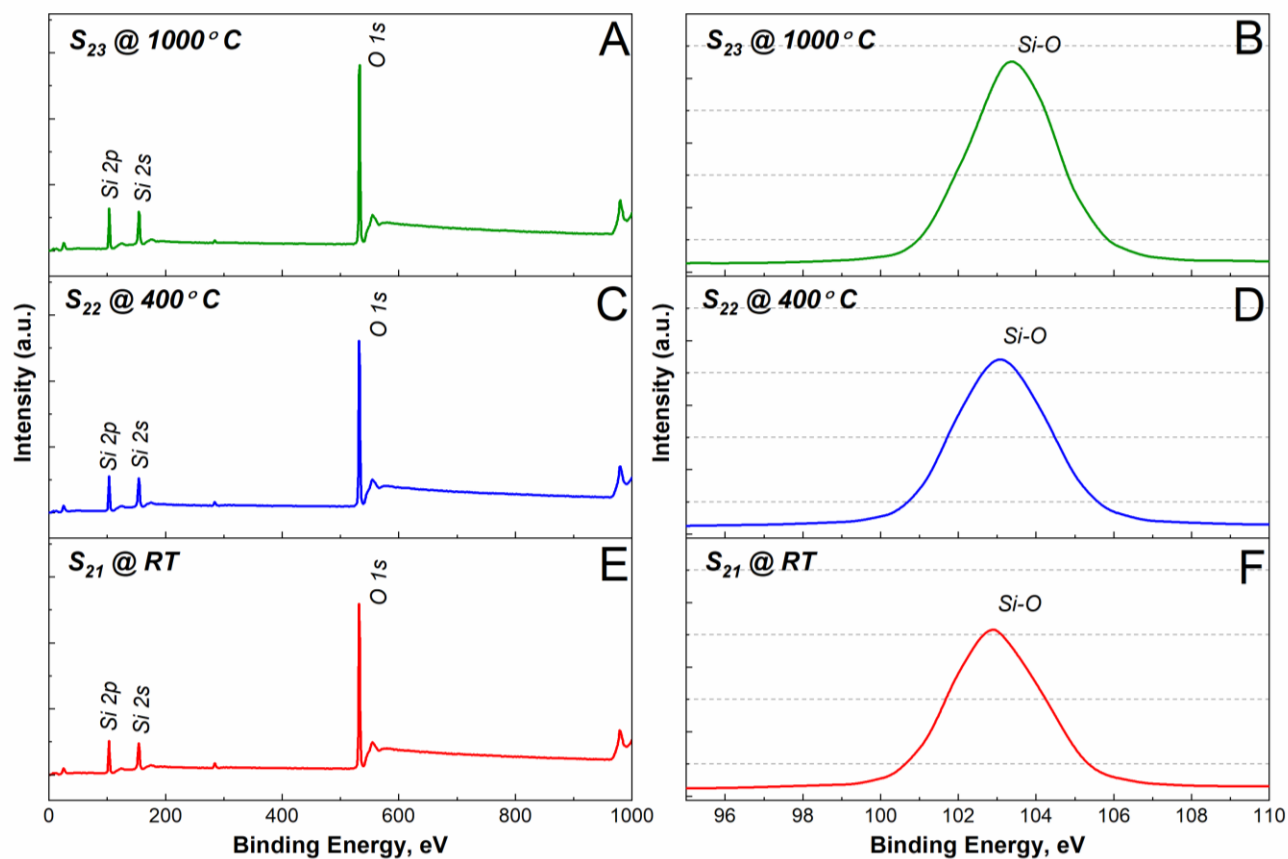


Fig. 4-6 XPS survey spectra of group2 samples, 1200kHz, (A,C,E) and XPS narrow cut spectra and chemical state analysis for the Si 2p region at ~103 eV, (B,D,F)

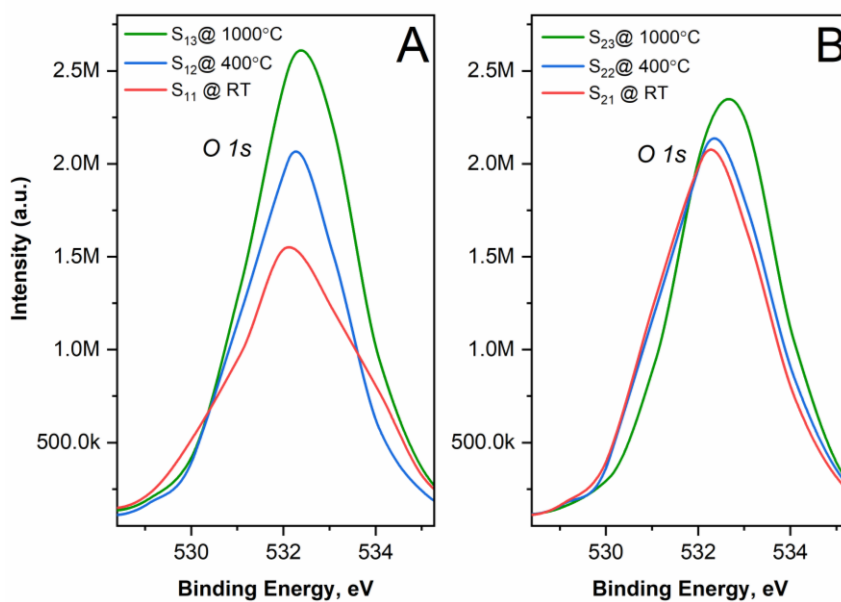


Fig. 4-7 O 1s XPS spectra before and after treatment for Group1 (A) and Group2(B) samples

X-ray diffraction (XRD) pattern nano-layers were inspected to confirm the crystallographic structure (Fig. 4-8 & Fig. 4-9). These figures (Fig. 4-8, Fig. 4-9) reveal that major peaks of silicon correspond to the crystallographic plane (111), (100), (220), (311) as identified by using the reported data [134].

XRD curves in Fig. 4-8 & Fig. 4-9 verify an amorphous hump at the (100) position on the surface in the as-prepared sample that changes to a prominent peak in the 400°C heated samples. Moreover, stronger crystallinity peaks can be seen in the 1000°C heated samples (S13, S23 in Fig. 4-8, Fig. 4-9) except for crystal planes at (100) which returned to a wider amorphous hump for S13. The polycrystalline structure of the S13 and S23 samples compared to the less crystalline S12 and S22 samples justify the order of the curves in reflection spectra.

Oxidation and crystallinity are key factors in shaping the reflection behavior. While slight oxidation is seen below 700°C in S12 and S22 [135], crystalline structure improvements for S12 and S22 shown in Fig. 4-8 & Fig. 4-9 respectively caused the reflection spectra to rise for treated samples at 400°C. XPS results (Fig. 4-7) show that samples heated at 1000°C (S13, S23) are more oxidized compared with the 400°C samples (S12, S22). Our previous work shows that oxidation results in more absorption and reduction both in transmission and reflection spectra [120]. An obvious poly-crystallinity increase adds to the oxidation effect for 1000°C treated samples' intensity drop in reflection spectra (Fig. 4-3). Multiple crystal planes return reflexes at diverse angles on one side and may increase the absorption on the other side. This is currently unclear and would be the subject of future investigation.

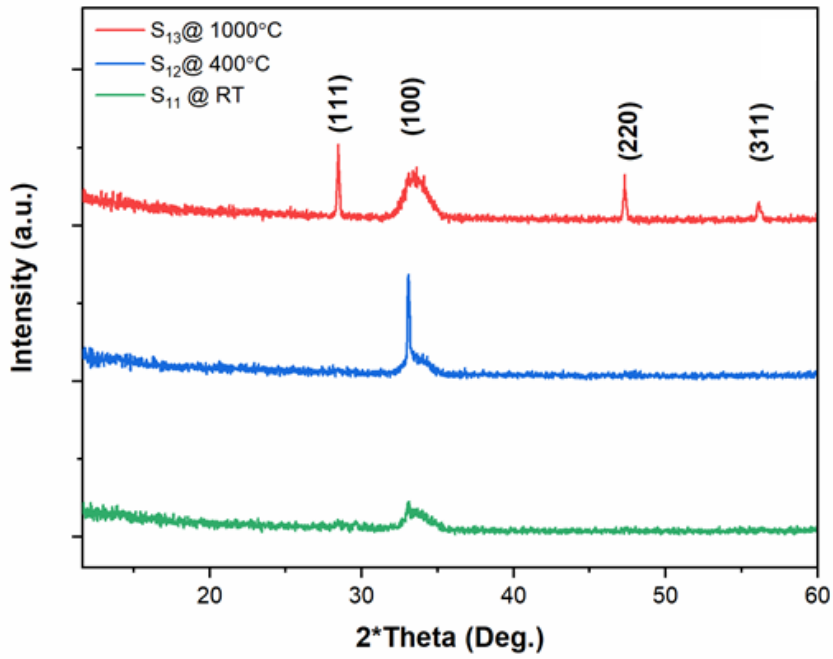


Fig. 4-8 XRD patterns of thin films with Si substrate (A) Magnified XRD spectrum of the thin film (B) for Group1 samples

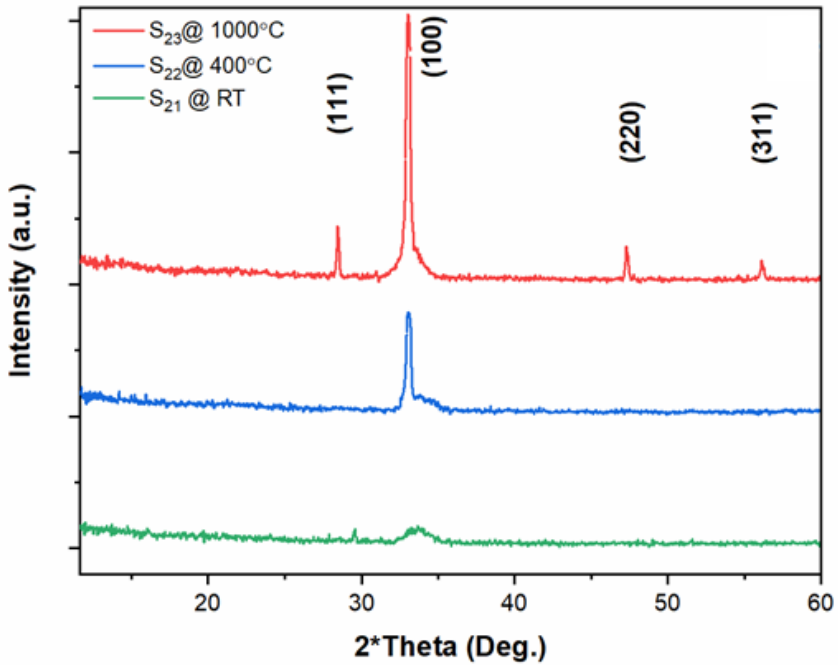


Fig. 4-9 XRD patterns of thin films with Si substrate (A) Magnified XRD spectrum of the thin film (B) for Group2 samples

#### 4.4 Conclusion

In this chapter reflection behavior of heat-treated thin films created by frequency variation was investigated. Frequency change leads to the generation of two different nanostructures ranging from particulate agglomerated to finely fibro-porous. The latter showed notable robustness and stability to heat treatment by a minimum variation and make this group of films a good candidate in application.

## Chapter 5.

### 3<sup>rd</sup> Study: Thin film real-time emissivity research<sup>3</sup>

#### 5.1 Introduction

The emissivity ( $\epsilon$ ) of a substance is the ratio of the energy radiated by a material to the energy radiated by a blackbody at the same temperature. Highly emissive thin films have received great attention recently, especially for spacecraft applications [136-137], radiative cooling applications [138], and electrical insulation [139]. There have been efforts in recent years to develop appropriate thermal sources for infrared (IR) related applications such as sensors for early detection of gas leakages. An essential component of all spectroscopic systems is the radiation source. In general, high-temperature thermal emitters are used as IR sources due to the high output power that can be obtained in a broadband spectral region, from the shorter to the larger IR wavelengths. Ceramic- or silicon-based IR emitters are also commonly used as thermal sources; their emissivity at larger wavelengths is close to the blackbody radiation but still broadband. Therefore, an intermediate composition such as SiO<sub>2</sub> or specific nanostructure is needed to tune this radiation, absorbing heat and selectively reemitting IR light in the desired band with the most efficient emissivity [140-141]. Theoretical modeling and experimental studies in this field of optical properties of nanostructured silicon have attracted a lot of attention because of its wide range of applications from sensors and emitters to biomedical and photonic devices [142-145].

On the other end, controlling thermal radiative properties of coatings materials in photovoltaic devices is important because as the temperature increases, the conversion efficiency of the solar cells and the lifetime of the material decreases. To overcome this problem, a highly emissive coating is deposited on the surface to effectively decrease the temperature by radiation [146]. Similarly, applying a high emissivity coating on a furnace wall increases the net temperature in the interior of the furnace, which ultimately helps to save electric power consumption [147].

---

<sup>3</sup> The results have been submitted to the Nanomaterial journal (figures will appear in that paper)

Emittance is an important material property that enables determination of the emissive power of a real body. Thermal radiation emission is a direct result of vibration and rotational motions of molecules, atoms, and electrons of a substance. Temperature is a measure of these activities. Thus, the rate of thermal radiation emission increases with increasing temperature. What we call light is the visible portion of the electromagnetic spectrum which lies within the thermal radiation band, but thermal emission is mostly in the infrared range [141, 146]. However, for opaque solids such as metals, radiation is considered to be a surface phenomenon, since the radiation emitted by the interior region never reaches the surface. Note that the radiation characteristics of surfaces can be changed completely by applying thin layers of coatings on them. In the literature, silicon oxide is among the many high emissivity coating materials, reported effective for thermal protection of solar cells, spacecraft, and energy-saving applications for industrial furnaces (to lower the surface temperature) [147]. When radiation falls on a body, it may be partially reflected, transmitted, or absorbed. The light penetration depth ‘ $d_p$ ’ is defined as the inverse of the absorption coefficient ( $\alpha$ ) and is closely related to the emissivity of the coating, which in turn depends on the wavelength ( $\lambda$ ) of the light and the extinction coefficient ( $k$ ) [148]:

$$d_p = \frac{1}{\alpha} = \frac{\lambda}{4\pi k} \quad (5-1)$$

Equation (5-1) suggests that penetration depth is inversely proportional to  $k$ . Therefore, a material with high penetration depth is required to achieve high emissivity. SiO<sub>2</sub> has a low extinction coefficient and a determinant to be observed in emissivity [148, 149].

In this research, we investigated the effect of Si/SiO<sub>2</sub> nanofiber density and the nature of film structure, either as agglomerated or nano-sized wired, on radiation emissions at two elevated temperatures. Characterizing techniques, scanning electron microscopy (SEM), micro-Raman, and X-ray photoelectron spectroscopy (XPS) was used to expand the results and emission enhancement mechanisms.

## 5.2 Sample preparation

Nine samples were generated by varying the frequencies (600kHz, 900kHz, 1200kHz) of the laser and the scanning speeds (10mm/s, 100mm/s, 200mm/s) of the galvo scanner (Table 5-1) on the silicon substrate. Frequency variation – in increasing order – led to samples from

particulate to nanofibers and fine nanofibers. Decreasing the scanning speed helped a generation of high, medium, and low amounts of nanofibers in 3D porous structure.

Table 5-1 Nanofabrication parameters and sample quantity

Group No.	Variable Parameter	Value	Fixed parameters	laser	Heat-up Temp.
1	Frequency	600 kHz	SS = 100 mm/s P = 10 W Pulse width= 150 ps Under ambient conditions		200°C & 350°C
		900 kHz			
		1200 kHz			
2	Scanning speed (SS)	10 mm/s	Frequency = 1200 kHz P = 10 W Pulse width= 150 ps Under ambient conditions		
		100 mm/s			
		200 mm/s			

Samples were heated on a hot plate to 200°C and 350°C while the reflection probe was kept at a fixed distance above them and measurements performed at tabulated elevated temperatures with a NIR range spectrometer. Figure 5-1 is a schematic of the experimental setup.

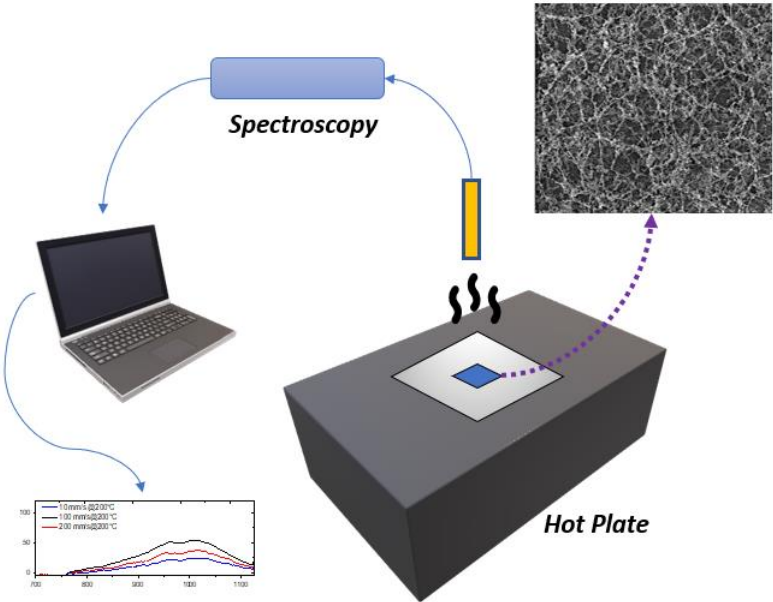


Fig. 5-1 Experimental setup: hot plate, spectroscopy, source light, and reflection probe

In measuring the radiance of the nanostructures, the fractions due to the bare substrate (slide glass) and ambiance have been subtracted and a black carbide sample, geometrically similar

to slide glass, was used as the black body reference in our presented results. Difficulties in measuring emissivity with small uncertainties also confronted us, such as keeping the probe-sample distance constant and fast data acquisition at the target temperature to avoid overheating damage and functional errors in the reflection probe.

### 5.3 Results and Discussion

Up to 60°C there were not any sensible changes in the measured spectra. Fig. 5-2 shows the radiation spectra at 50°C for frequency variations that are mostly indistinguishable against wavelength. We observed the same behavior for the samples prepared at varied scanning speeds.

Fig. 5-2 show the reflection spectra of samples synthesized by frequency and scanning speed variation respectively. Bare substrate radiation is subtracted from acquired data. Emission is increased over wavelength for higher pulsed laser frequencies in the NIR range.

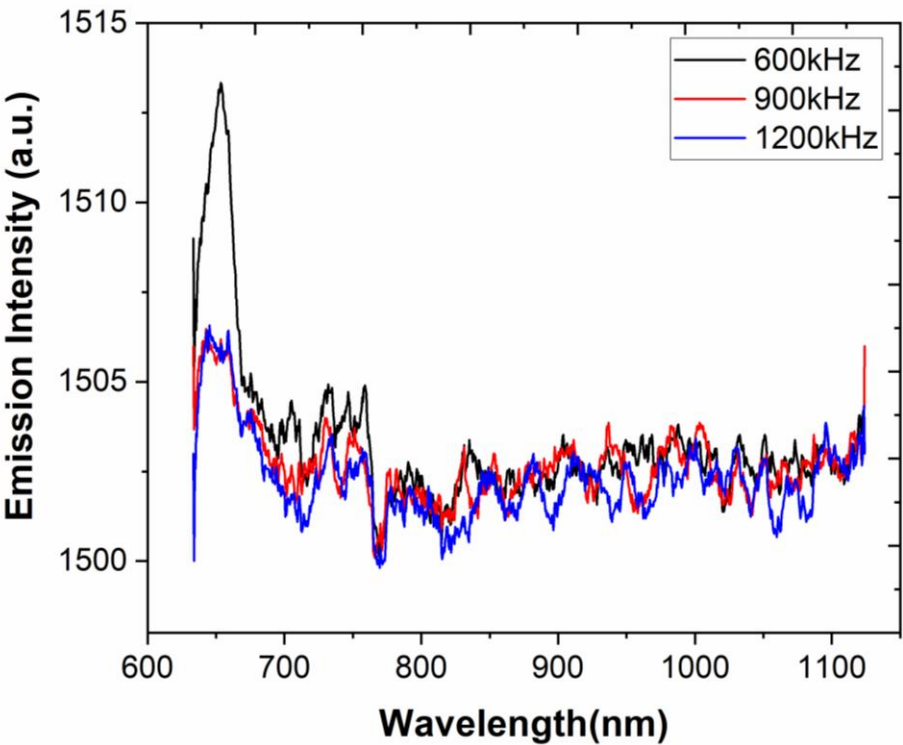
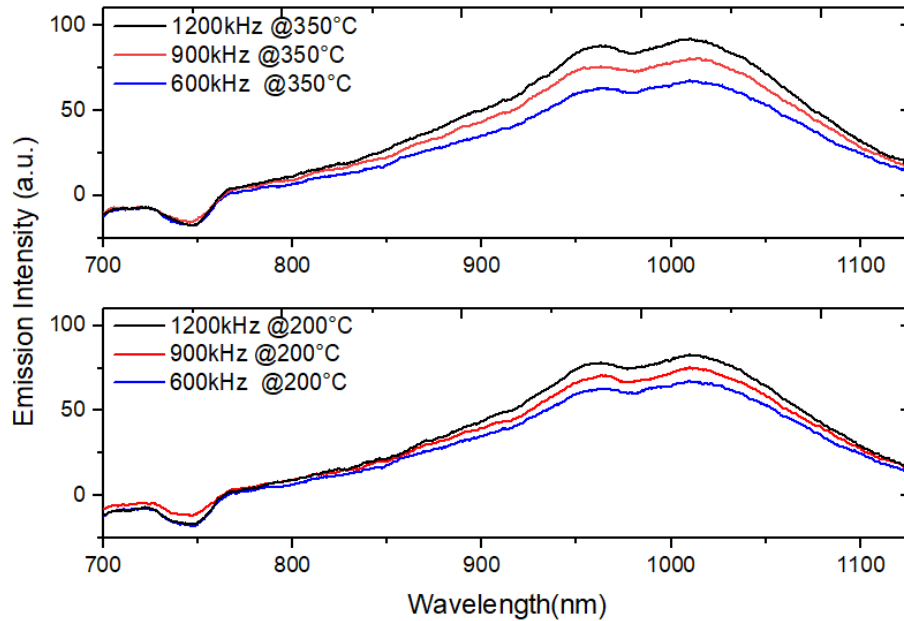


Fig. 5-2 Frequency varied samples with no distinguishable change in emission at 50°C



*Fig. 5-3 Emission measured at 200°C and 350°C from frequency varied samples*

Emission intensity increased with rising frequency and for each set of manufacturing parameters with temperature rise, as expected. As previously reported [120], the thickness of the laser-generated thin-film slightly increasing from  $16.5$  to  $23 \mu\text{m} \pm 10\%$  by decreasing the laser frequency from  $1200$  to  $600$  kHz; in another research by Edalatpour and Francoeur [151], it has been revealed that emissivity of dielectrics films decreases as the film thickness decreases due to a loss of source volume; However, because of the high porosity of the laser-generated thin-film structures and its high internal light trapping, the measured radiance is governed by the thin-film porous structures and is mainly corresponding to the emissivity from the surface.

The development of a porous and nanofibrous structure by increasing the laser pulse frequency caused a higher contact surface area as illustrated in the SEM results (Figure 5-4). The higher emission at raised temperatures can be attributed to the vast surface area mentioned above [152]. Yu et al. [153] proposed a theoretical model to elaborate on the effect of porosity on emissivity. According to the results, a high porosity in the coating helps boost emissivity. In this case, the oxidation level observed in the Raman scattering spectrum for samples at  $\sim 1100 \text{ cm}^{-1}$  follows the same trend as the silicon peak at  $\sim 520 \text{ cm}^{-1}$  (Figure 5-5) and 3D surface morphology confirms the emissivity rise with frequency increase. As

reported before [153], by increasing the laser repetition rate, the average surface temperature decreases; thus, the amount of nan-oxidized silicon (in the form of amorphous Si(a-Si)) increases. The secondary peak at the wavenumber of  $480\text{ cm}^{-1}$  in the  $1200\text{ kHz}$  frequency (Figure 5-5), is the characteristic for the formed amorphous silicon [154].

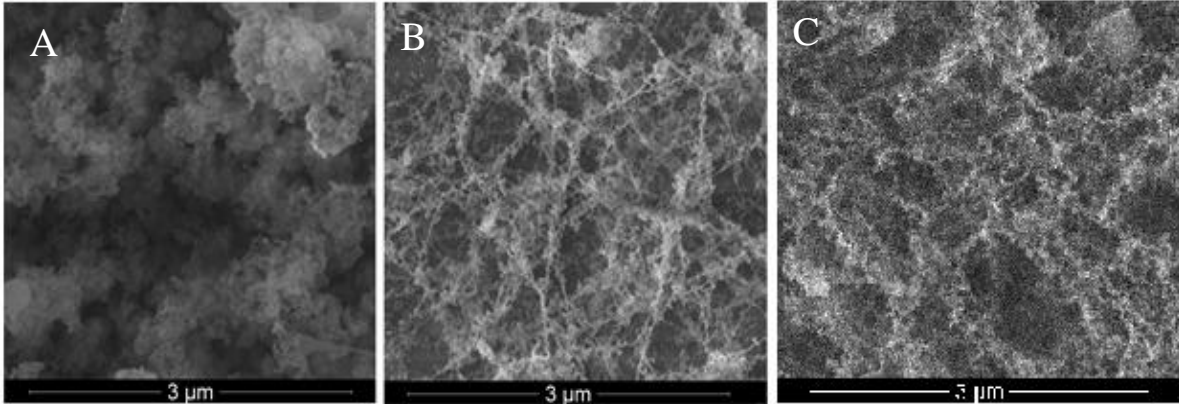


Fig. 5-4 SEM images of samples synthesized at A) 600kHz, B) 900kHz, C) 1200kHz

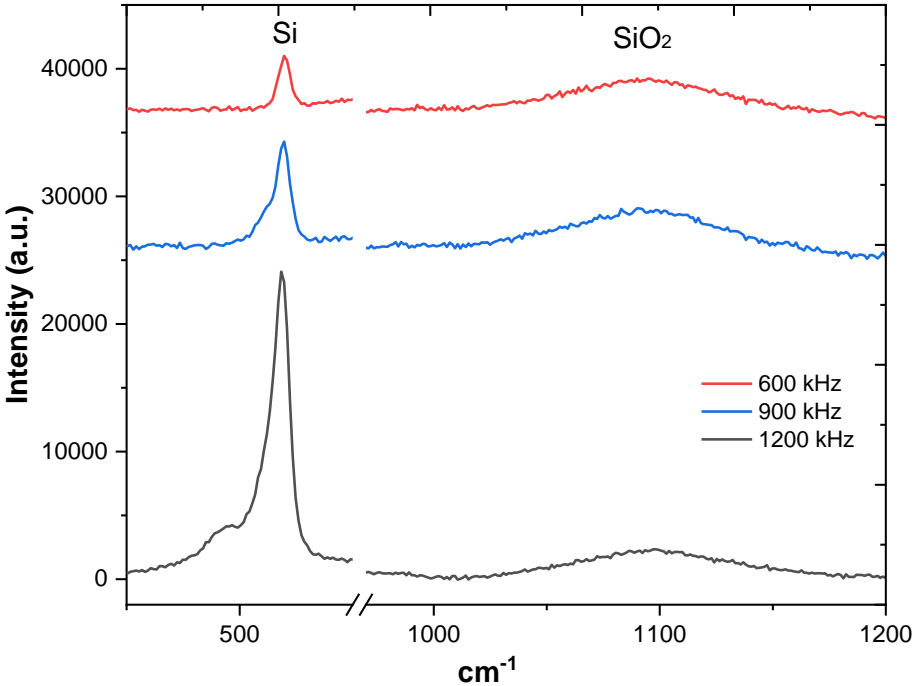


Fig. 5-5 Raman spectra in the vicinity of Si/SiO<sub>2</sub> peak for frequency variation

Figure 5-6 shows emission intensity elevation with scanning speed reduction and expectedly for each speed with temperature increase from  $200$  to  $400^\circ\text{C}$ . Lower speeds cause higher

ablated material removal and consequently a thicker deposited layer on the substrate. SEM images (Figure 5-7) verify the increased density of the nanofibrous structures on samples made inversely proportional to scanning inscription speed. Such structures provide significant contact interfaces with the outside and improve heat radiation from the thin films. The emission mechanism concerning material characteristics, Raman in this case, is different from the frequency varied samples. Oxidation as SiO<sub>2</sub> content increases with slower scanning speeds (Figures 5-5 to 5-8 at  $\sim 1100\text{ cm}^{-1}$ ), is a determining factor in the buildup of emission intensity [148, 155].

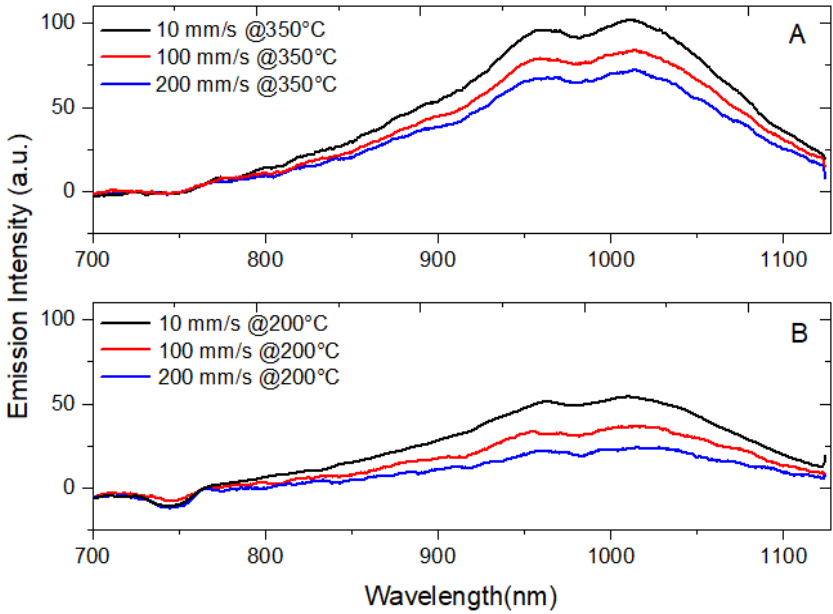


Fig. 5-6 Emission measured at 200°C and 350°C from frequency varied samples

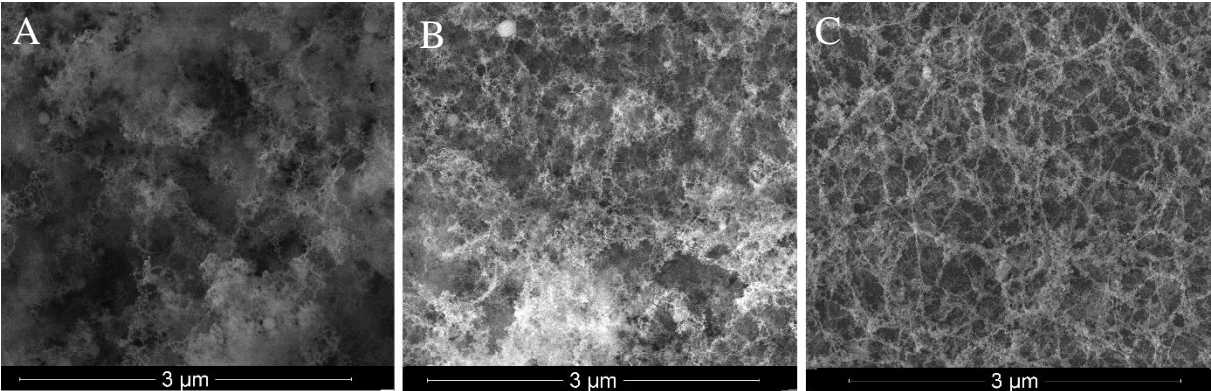
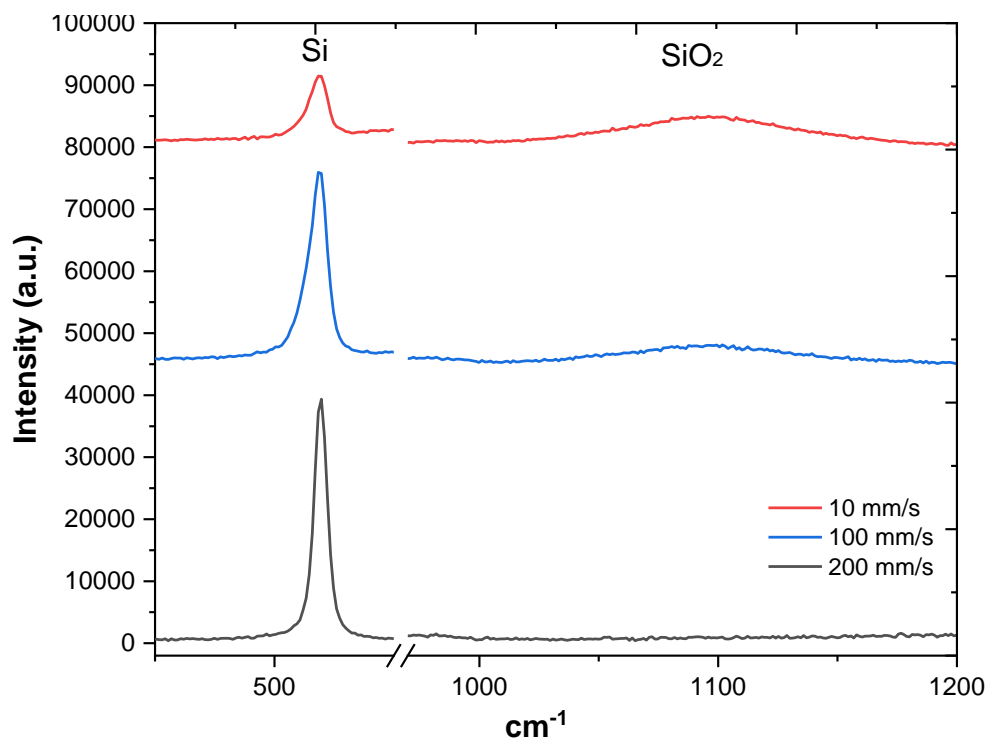


Fig. 5-7 SEM images of samples synthesized at A) 10mm/s, B) 100mm/s, C) 200mm/s



*Fig. 5-8 Raman spectra in the vicinity of Si/SiO<sub>2</sub> peak for scanning speed variation*

Complementary information about the relative elemental and chemical composition of the nanostructures was obtained from XPS analysis before heating the samples. In Figure 5-9 deconvolution of the Si2p XPS peak of speed varied samples confirms the presence of two silicon suboxide peaks, Si<sup>3+</sup>, an elemental silicon peak, and an Si<sup>4+</sup> peak indicative of fully oxidized silicon. This elemental silicon sub-peak is due to silicon nano-inclusions within the oxide layer, and its large contribution together with the small Si<sup>4+</sup> (i.e., SiO<sub>2</sub>) contribution confirms that the oxide is silicon-rich. The fitted peaks have binding energies (BE) of 102.7 eV at (Si<sup>3+</sup>) and 103.9 eV at (Si<sup>4+</sup>). The large contribution from Si<sup>3+</sup> suggests a high concentration of asymmetrical SiO<sub>2</sub>≡Si-Si and O<sub>3</sub>≡Si-Si species [157].

The quantum theory shows that the radiation emission is the result of interaction between molecular transition dipoles and oscillating electric fields essentially, which is correlated with the vibration of the crystal structure. Stronger lattice vibration would lead to greater emissivity.

Therefore, varied oxide phases decrease the symmetry of lattice vibrations in turn, and enhance the effects of the anharmonic vibration of polar lattices, coupled action of phonons,

and phonon combination radiation [156, 157]. Therefore, the emissivity considerably increases when the speed decreases from 200 mm/s to 10 mm/s.

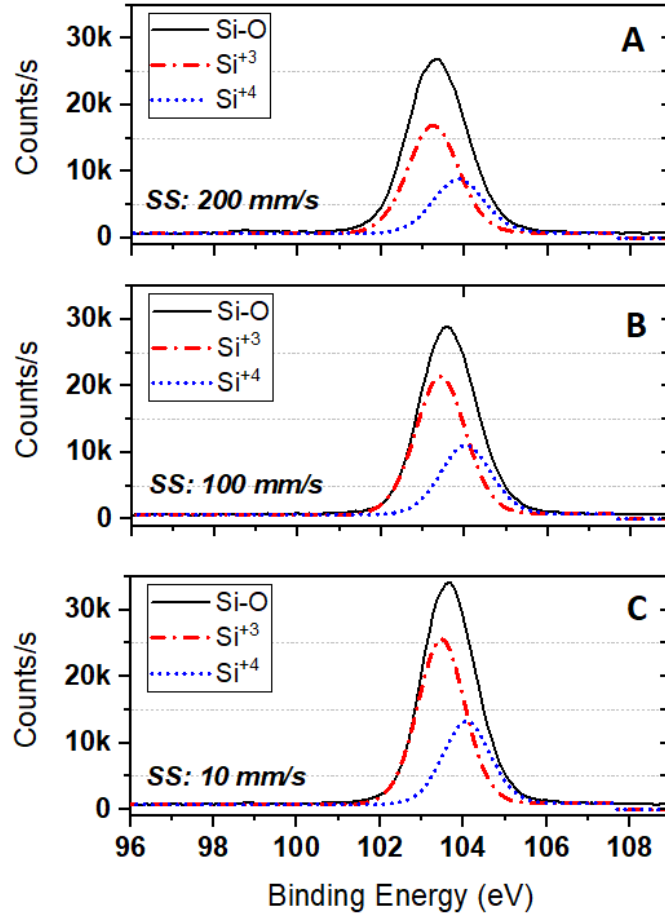


Figure 5-9 Si<sub>2p</sub> XPS spectrum of thin films, showing the presence of Si<sup>3+</sup> and Si<sup>4+</sup> configurations at scanning speeds A)200 mm/s B)100 mm/s and C)10 mm/s.

XPS was also performed to identify the evolution of surface chemical composition for frequency varied samples (Figure 5-10). The binding energy of Si(2p) peaks are the same as mentioned earlier, plus 101.6 eV for Si<sup>2+</sup> that exhibit markedly high intensities for 600 kHz and 900 kHz. The total oxidation levels (black lines) are almost the same for different frequencies, which conform to the balanced Raman scattering results. As we previously reported [153], the average surface temperature (it is different from the maximum temperature which accurs at the end of each pulse) increases from 500K to 700K by decreasing the frequency from 600 kHz to 1200 kHz. The increase in the average surface temperature is still below the oxidation temperature threshold. However, by varying the

scanning speed from 200 mm/s to 10 mm/s, the average surface temperature surpassed the oxidation threshold which are in good agreements with our Raman and XPS results.

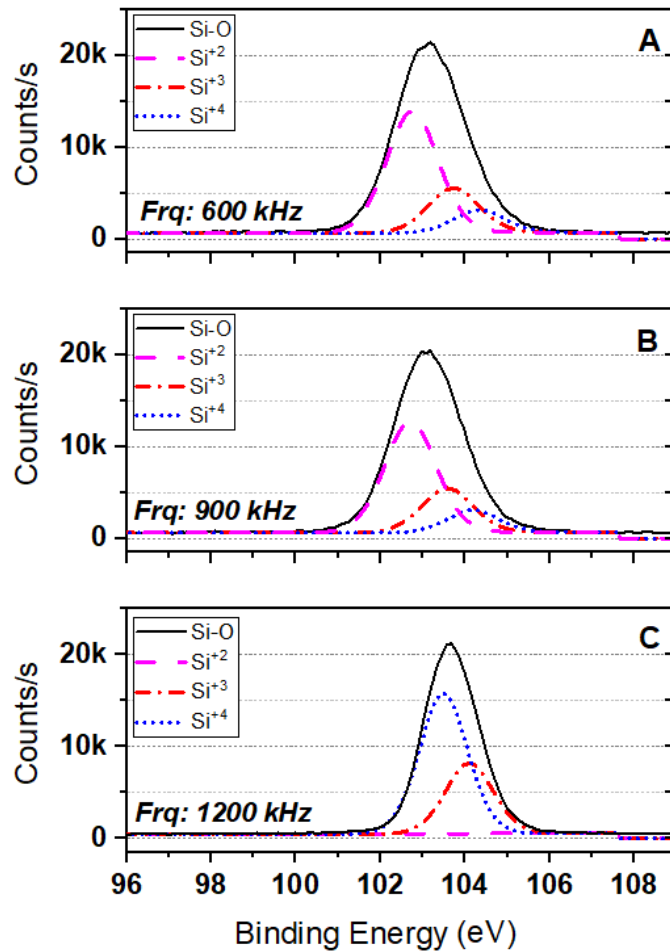


Figure 5-10 Si<sub>2p</sub> XPS spectrum of films, showing the presence of Si<sup>2+</sup>, Si<sup>3+</sup> and Si<sup>4+</sup> configurations at scanning speeds A)600 kHz B)900 kHz and C)1200 kHz.

#### 5.4 Conclusion

Emissivity needs to be studied in many applications so we explored radiation for two groups of samples generated by altering scanning speed and frequency of a pulsed laser. Measurements were performed on heated samples at two temperatures in real-time. High contact surface area caused by the fibro-porous structure and the oxidation phases were the determining factors in the emissivity and radiation of the samples.

## Chapter 6.

### Outcome and Outlook

#### 6.1 Closing remark

Silicon and its derivatives like SiO<sub>2</sub> are essential materials for industrial applications such as semiconductors, optoelectronics, and telecommunication. They are demanding in thin and porous structures products and even more with fine nanofibrous morphology. By capable fabrication techniques as in laser ablation they can be utilized for novel applications. The three main studies in this thesis intend to address the impact of manufacturing factors and post-treatment on selective optical features of a large group of samples.

In the first study, pulsed-laser determinants were changed to investigate the Vis-NIR attributes of generated thin films. In most cases, SEM verified dominant fibrous structures, except for the sample that was fabricated at a low frequency of 600 kHz.

Our results show that physical and chemical properties, namely porosity, nanofibrous morphology, and oxidation level, play an important role in the optical properties of the generated thin films. Power increases (6.5 to 15 W) directly affect material removal rate and oxidation quantity in making more porous structures. Frequency increases (600 to 1200 kHz) lead to lower silica levels and denser nano-wired thin film, with its maximum at 1200 kHz. Pulse duration increases (150 ps to 5 ns), boosted silicon concentration in deposited material while degrading the fibrous structure and reducing measured intensities. Faster scanning speeds (10 to 200 mm/s) reduced the film thickness independently and lowered the level of oxidation that would result in more light transmittance. The thickest film, which was notably off-trend, occurred at 10 mm/s.

In the second study heated and as-deposited Si/SiO<sub>2</sub> nanostructured films were generated by pulsed laser deposition and studied for their visible range reflection behavior. Our results show that physical and chemical properties, namely surface morphology, oxidation, and prominent bondings and crystallinity affect the observed optical properties. Characterization techniques such as SEM, XPS, and XRD were employed to explain the trends. Two differently generated groups of samples exhibited more and fewer reflection intensities than the as-deposited ones. The fibro-porous samples showed resistance to variation about the

as-prepared sample while the distribution of particulate samples varied notably. Heat treatments lower than 700°C led to a single crystalline structure that governed high reflection response, but polycrystallinity was the determiner for 1000°C low reflection intensities. The results of this study can lead to promising solutions for the fabrication of better optical structures with tuned optical properties which can be used in the wide range of applications from photonics to bio and chemical sensor fabrications.

Third study focuses on the effects of the nature of nanostructure, density of fibers and compositional constituents on the improvement of emissivity for heated samples. Frequency of the laser and scanning speeds were variables of nanofabrication that were used to generate particulate to nanofibrous and remarkably porous thin coatings. SEM images confirmed particulate formation for a 600 kHz repetition rate and fibrous topography for the rest of the frequencies and scanning speeds. SEM images along with Raman and XPS results showed how extremely and high interfacing surface made the most from nanofibrous structure to improve the emission of frequency varied samples. However, oxidation phases along with the advantageous high contact surface area accommodate higher emissivity by reducing the scanning speed. In general, by both increasing the frequency from 600 kHz to 1200 kHz and reducing the scanning speed from 200 mm/s to 10 mm/s, we can increase the emissivity of the laser-induced nanofibrous structures. However, the effect of laser scanning speed is more significant and enables us to vary the emissivity in the higher range as it takes advantage of both higher surface area and higher oxidation range. Our results can open new doors for the fabrication of novel emitting nanostructured thin-film for a wide range of applications for photovoltaic, aerospace, and nanophotonic devices.

A big picture of the results shows the potential for choosing reasonable estimates of manufacturing parameters to create thin films with required characteristics. In all cases, the extremely high internal surface area of nanofibrous silicon, the ease in modifying the surface chemistry of PSi, and the straightforward fabrication of PSi films are key advantages for the generated structures.

Observation of these trends enabled us to apply tunable fabrication procedures to obtain desired groups of nanofibrous thin films. Electron and optical microscopy, as well as background knowledge, certify tangled nano-wired morphology in most cases. Structures

with highly desirable usages, such as in sensing technology, can be optimized by their porosity, density, and thickness.

## 6.2 Future Perspective

In recent years, the use of PSi as a high surface area host for various materials is being studied to generate improved sensing platforms and dual-mode biosensors. While in the previous decade polymers and hydrogels were the focus points.

Furthermore, the optical properties of nanofibrous structures can be utilized simultaneously with embedded light-emitted species, generating dual-mode biosensing platforms. In addition, metal-coated PSi generates SERS-active substrates, which have shown a great promise with a significant Raman enhancement factor, long storage stability and signal repeatability. Progression of research in these directions is anticipated to continue in the following years.

Biosensors are amongst the largest markets which are anticipated to reach \$27.06 billion by 2022 [141]. They are significantly demanding in the point-of-care (POC) diagnostics field that provides technology solutions alternatives to the expensive, time-consuming, bulky, and lab-confined traditional analytical methods of carrying out molecular detection.

Tuneable properties of our samples are particularly appealing for the design of in vitro and in vivo biomedical materials:

- The high surface area that can be functionalized by a wide range of chemical and biological species
- Photonic properties for label-free biosensing and for self-reporting drug delivery
- Inexpensive and rapid fabrication techniques with the ability to further process into thin membranes and micro- or nano-particles
- Biocompatible degradation into noninflammatory bioproduct silicic acid ( $\text{Si(OH)}_4$ ) species and likewise compounds

## References

1. Canham, L., *Handbook of porous silicon*. 2014: Springer.
2. Moreno, M. and P.R. i Cabarrocas, *Ultra-thin crystalline silicon films produced by plasma assisted epitaxial growth on silicon wafers and their transfer to foreign substrates*. EPJ Photovoltaics, 2010. **1**: p. 10301.
3. Cullis, A., L. Canham, and O. Dosser, *The structure of porous silicon revealed by electron microscopy*. MRS Online Proceedings Library Archive, 1991. **256**.
4. Uhler Jr, A., *Electrolytic shaping of germanium and silicon*. Bell System Technical Journal, 1956. **35**(2): p. 333-347.
5. Archer, R., *Stain films on silicon*. Journal of Physics and Chemistry of Solids, 1960. **14**: p. 104-110.
6. Theunissen, M., *Etch Channel Formation during Anodic Dissolution of N-Type Silicon in Aqueous Hydrofluoric Acid*. Journal of the Electrochemical Society, 1972. **119**(3): p. 351.
7. Canham, L. and A. Groszek, *Characterization of microporous Si by flow calorimetry: Comparison with a hydrophobic SiO<sub>2</sub> molecular sieve*. Journal of applied physics, 1992. **72**(4): p. 1558-1565.
8. Hummel, R. and S.S. Chang, *Novel technique for preparing porous silicon*. Applied physics letters, 1992. **61**(16): p. 1965-1967.
9. Noguchi, N. and I. Suemune, *Luminescent porous silicon synthesized by visible light irradiation*. Applied physics letters, 1993. **62**(12): p. 1429-1431.
10. Savin, D., et al., *Properties of laser ablated porous silicon*. Applied physics letters, 1996. **69**(20): p. 3048-3050.
11. Chen, Q., et al., *Ultraviolet light emission from porous silicon hydrothermally prepared*. Physics Letters A, 1996. **224**(1-2): p. 133-136.
12. Dimova-Malinovska, D., et al., *Preparation of thin porous silicon layers by stain etching*. Thin Solid Films, 1997. **297**(1-2): p. 9-12.
13. Ashruf, C., et al., *Galvanic porous silicon formation without external contacts*. Sensors and Actuators A: Physical, 1999. **74**(1-3): p. 118-122.
14. Kalkan, A.K., et al., *Biomedical/analytical applications of deposited nanostructured Si films*. Nanotechnology, 2005. **16**(8): p. 1383.
15. Saadoun, M., et al., *Vapour-etching-based porous silicon: a new approach*. Thin Solid Films, 2002. **405**(1-2): p. 29-34.
16. Kabashin, A. and M. Meunier, *Fabrication of photoluminescent Si-based layers by air optical breakdown near the silicon surface*. Applied surface science, 2002. **186**(1-4): p. 578-582.
17. Beydaghyan, G., et al., *Enhanced birefringence in vacuum evaporated silicon thin films*. Applied optics, 2004. **43**(28): p. 5343-5349.
18. Nakahata, T. and H. Nakajima, *Fabrication of lotus-type porous silicon by unidirectional solidification in hydrogen*. Materials Science and Engineering: A, 2004. **384**(1-2): p. 373-376.
19. Abdi, Y., et al., *Light-emitting nano-porous silicon structures fabricated using a plasma hydrogenation technique*. Materials Science and Engineering: B, 2005. **124**: p. 483-487.

20. Fukutani, K., et al., *Characterization of nanoporous Si thin films obtained by Al–Si phase separation*. Applied Physics Letters, 2005. **87**(25): p. 253112.
21. Holtz, M., et al., *Optical properties of a nanoporous array in silicon*. 2004.
22. Voigt, F., et al., *Porous thin films grown from size-selected silicon nanocrystals*. Materials Science and Engineering: C, 2005. **25**(5-8): p. 584-589.
23. Bao, Z., et al., *Chemical reduction of three-dimensional silica micro-assemblies into microporous silicon replicas*. Nature, 2007. **446**(7132): p. 172-175.
24. Zheng, Y., et al., *Nano-porous Si/C composites for anode material of lithium-ion batteries*. Electrochimica acta, 2007. **52**(19): p. 5863-5867.
25. Jakubowicz, J., K. Smardz, and L. Smardz, *Characterization of porous silicon prepared by powder technology*. Physica E: Low-dimensional Systems and Nanostructures, 2007. **38**(1-2): p. 139-143.
26. Kim, H., et al., *Three-dimensional porous silicon particles for use in high-performance lithium secondary batteries*. Angewandte Chemie International Edition, 2008. **47**(52): p. 10151-10154.
27. Woldering, L.A., et al., *Periodic arrays of deep nanopores made in silicon with reactive ion etching and deep UV lithography*. Nanotechnology, 2008. **19**(14): p. 145304.
28. Mahmood, A.S., et al., *Enhancement in optical absorption of silicon fibrous nanostructure produced using femtosecond laser ablation*. Applied physics letters, 2009. **95**(3): p. 034107.
29. Fang, D., et al., *Methods for controlling the pore properties of ultra-thin nanocrystalline silicon membranes*. Journal of Physics: Condensed Matter, 2010. **22**(45): p. 454134.
30. Truong, D.C., et al., *Effect of temperature in electrochemical texturising of multi-crystalline silicon in KOH solution*. International journal of nanotechnology, 2013. **10**(3-4): p. 288-295.
31. Krishnamurthy, A., D.H. Rasmussen, and I.I. Suni, *Galvanic deposition of Nanoporous Si onto 6061 Al alloy from aqueous HF*. Journal of The Electrochemical Society, 2011. **158**(2): p. D68-D71.
32. Skorb, E.V., D.V. Andreeva, and H. Möhwald, *Generation of a porous luminescent structure through ultrasonically induced pathways of silicon modification*. Angewandte Chemie International Edition, 2012. **51**(21): p. 5138-5142.
33. Yang, X., et al., *Porous graphite/silicon micro-sphere prepared by in-Situ carbothermal reduction and spray drying for lithium ion batteries*. ECS Solid State Letters, 2012. **1**(2): p. M5.
34. Huang, X., et al., *Fabrication and size dependent properties of porous silicon nanotube arrays*. Chemical Communications, 2013. **49**(51): p. 5760-5762.
35. Wang, J.-F., et al., *Amorphous silicon with high specific surface area prepared by a sodiothermic reduction method for supercapacitors*. Chemical Communications, 2013. **49**(44): p. 5007-5009.
36. Godinho, V., et al., *A new bottom-up methodology to produce silicon layers with a closed porosity nanostructure and reduced refractive index*. Nanotechnology, 2013. **24**(27): p. 275604.

37. Deng, T., et al., *Fabrication of inverted-pyramid silicon nanopore arrays with three-step wet etching*. ECS journal of solid state science and technology, 2013. **2**(11): p. P419-P422.
38. Li, X., et al., *Fast electroless fabrication of uniform mesoporous silicon layers*. Electrochimica Acta, 2013. **94**: p. 57-61.
39. Stepanov, A.L., et al., *Fabrication of nanoporous silicon by Ag<sup>+</sup>-ion implantation*. Nanoscience and Nanoengineering, 2013. **1**(3): p. 134-138.
40. Dai, F., et al., *Bottom-up synthesis of high surface area mesoporous crystalline silicon and evaluation of its hydrogen evolution performance*. Nature communications, 2014. **5**(1): p. 1-11.
41. Zhang, Z., et al., *Scalable synthesis of interconnected porous silicon/carbon composites by the rochow reaction as high-performance anodes of lithium ion batteries*. Angewandte Chemie, 2014. **126**(20): p. 5265-5269.
42. Wada, T., et al., *Bulk-nanoporous-silicon negative electrode with extremely high cyclability for lithium-ion batteries prepared using a top-down process*. Nano letters, 2014. **14**(8): p. 4505-4510.
43. Liang, J., et al., *Nanoporous silicon prepared through air-oxidation demagnesiumation of Mg 2 Si and properties of its lithium ion batteries*. Chemical Communications, 2015. **51**(33): p. 7230-7233.
44. Kaniukov, E.Y., et al., *Tunable nanoporous silicon oxide templates by swift heavy ion tracks technology*. Nanotechnology, 2016. **27**(11): p. 115305.
45. Liebes-Peer, Y., et al., *Fabrication of nanopores in multi-layered silicon-based membranes using focused electron beam induced etching with XeF<sub>2</sub> gas*. Microchimica Acta, 2016. **183**(3): p. 987-994.
46. Kolasinski, K.W., et al., *Regenerative electroless etching of silicon*. Angewandte Chemie International Edition, 2017. **56**(2): p. 624-627.
47. Lang, W., et al., *Application of porous silicon as a sacrificial layer*. Sensors and Actuators A: Physical, 1994. **43**(1-3): p. 239-242.
48. Lang, W., P. Steiner, and H. Sandmaier, *Porous silicon: a novel material for microsystems*. Sensors and Actuators A: Physical, 1995. **51**(1): p. 31-36.
49. Steiner, P. and W. Lang, *Micromachining applications of porous silicon*. Thin solid films, 1995. **255**(1-2): p. 52-58.
50. Bischoff, T., et al., *Frontside micromachining using porous-silicon sacrificial-layer technologies*. Sensors and Actuators A: Physical, 1997. **60**(1-3): p. 228-234.
51. Holke, A., et al. *Coherent macro porous silicon as a wick structure in an integrated microfluidic two-phase cooling system*. in *Microfluidic Devices and Systems*. 1998. International Society for Optics and Photonics.
52. Sim, J.-H., et al., *Eight-beam piezoresistive accelerometer fabricated by using a selective porous-silicon etching method*. Sensors and Actuators A: Physical, 1998. **66**(1-3): p. 273-278.
53. Lammel, G. and P. Renaud, *Free-standing, mobile 3D porous silicon microstructures*. Sensors and Actuators A: Physical, 2000. **85**(1-3): p. 356-360.
54. Kalinowski, T., et al., *An advanced micromachined fermentation monitoring device*. Sensors and Actuators B: Chemical, 2000. **68**(1-3): p. 281-285.

55. Lee, C.-S., J.-D. Lee, and C.-H. Han, *A new wide-dimensional freestanding microstructure fabrication technology using laterally formed porous silicon as a sacrificial layer*. *Sensors and Actuators A: Physical*, 2000. **84**(1-2): p. 181-185.
56. Benecke, W. and A. Splinter. *MEMS applications of porous silicon*. in *Device and Process Technologies for MEMS and Microelectronics II*. 2001. International Society for Optics and Photonics.
57. Kronast, W., et al., *Single-chip condenser microphone using porous silicon as sacrificial layer for the air gap*. *Sensors and Actuators A: Physical*, 2001. **87**(3): p. 188-193.
58. Dantas, M.O., et al., *Silicon field-emission devices fabricated using the hydrogen implantation-porous silicon (HI-PS) micromachining technique*. *Journal of microelectromechanical systems*, 2008. **17**(5): p. 1263-1269.
59. Liu, Z., et al., *Fabrication planar coil on oxide membrane hollowed with porous silicon as sacrificial layer*. *Sensors and Actuators A: Physical*, 2003. **108**(1-3): p. 112-116.
60. Mescheder, U., *Porous silicon: Technology and applications for micromachining and MEMS*, in *Smart Sensors and MEMS*. 2004, Springer. p. 273-288.
61. Ning, J., et al. *A silicon capacitive microphone based on oxidized porous silicon sacrificial technology*. in *Proceedings. 7th International Conference on Solid-State and Integrated Circuits Technology, 2004*. 2004. IEEE.
62. Valera, E., et al. *Microporous silicon for CMOS compatible MST*. in *Conference on Electron Devices, 2005 Spanish*. 2005. IEEE.
63. Rajaraman, S. and H. Henderson, *A unique fabrication approach for microneedles using coherent porous silicon technology*. *Sensors and Actuators B: Chemical*, 2005. **105**(2): p. 443-448.
64. Rajta, I., et al., *Si micro-turbine by proton beam writing and porous silicon micromachining*. *Nuclear Instruments and Methods in Physics Research Section B: Beam Interactions with Materials and Atoms*, 2009. **267**(12-13): p. 2292-2295.
65. Olivares, J., et al., *Porous silicon oxide sacrificial layers deposited by pulsed-direct current magnetron sputtering for microelectromechanical systems*. *Thin solid films*, 2010. **518**(18): p. 5128-5133.
66. Weisse, J.M., et al., *Electroassisted transfer of vertical silicon wire arrays using a sacrificial porous silicon layer*. *Nano letters*, 2013. **13**(9): p. 4362-4368.
67. Dang, Z., et al., *Silicon and porous silicon mid-infrared photonic crystals*. *Applied Physics A*, 2013. **112**(3): p. 517-523.
68. Rittersma, Z., et al., *A novel surface-micromachined capacitive porous silicon humidity sensor*. *Sensors and Actuators B: Chemical*, 2000. **68**(1-3): p. 210-217.
69. Misra, S., R. Bhattacharya, and R. Angelucci, *Integrated polymer thin film macroporous silicon microsystems*. *Journal of the Indian Institute of Science*, 2013. **81**(5): p. 563.
70. De Stefano, L., et al., *Time-resolved sensing of chemical species in porous silicon optical microcavity*. *Sensors and Actuators B: Chemical*, 2004. **100**(1-2): p. 168-172.
71. De Stefano, L., et al., *A microsystem based on porous silicon-glass anodic bonding for gas and liquid optical sensing*. *Sensors*, 2006. **6**(6): p. 680-687.

72. De Stefano, L., et al., *Porous silicon-based optical biochips*. Journal of Optics A: Pure and Applied Optics, 2006. **8**(7): p. S540.
73. De Stefano, L., et al., *DNA optical detection based on porous silicon technology: from biosensors to biochips*. Sensors, 2007. **7**(2): p. 214-221.
74. De Stefano, L., et al., *An integrated hybrid optical device for sensing applications*. physica status solidi c, 2007. **4**(6): p. 1946-1950.
75. De Stefano, L., et al., *An integrated pressure-driven microsystem based on porous silicon for optical monitoring of gaseous and liquid substances*. physica status solidi (a), 2007. **204**(5): p. 1459-1463.
76. De Stefano, L., et al., *Optical microsystems based on a nanomaterial technology*. Journal of Physics: Condensed Matter, 2007. **19**(39): p. 395008.
77. Longo, A., A. Diligenti, and G. Barillaro, *A Minimally Invasive Microchip for Transdermal Injection/Sampling Applications*. 2012.
78. Barillaro, G., et al., *Integrated optofluidic microsystem based on vertical high-order one-dimensional silicon photonic crystals*. Microfluidics and nanofluidics, 2012. **12**(1-4): p. 545-552.
79. McInnes, S.J., et al., *Combination of iCVD and porous silicon for the development of a controlled drug delivery system*. ACS applied materials & interfaces, 2012. **4**(7): p. 3566-3574.
80. Paladiya, C. and A. Kiani. *Synthesis of Graphite Embedded SiO<sub>2</sub> Nanofibers with Controlled Conductivity*. in *2018 Photonics North (PN)*. 2018. IEEE.
81. Vo-Dinh, T. and B. Cullum, *Biosensors and biochips: advances in biological and medical diagnostics*. Fresenius' journal of analytical chemistry, 2000. **366**(6-7): p. 540-551.
82. Lim, D.V., *Detection of microorganisms and toxins with evanescent wave fiber-optic biosensors*. Proceedings of the IEEE, 2003. **91**(6): p. 902-907.
83. Mello, L.D. and L.T. Kubota, *Review of the use of biosensors as analytical tools in the food and drink industries*. Food chemistry, 2002. **77**(2): p. 237-256.
84. Nirschl, M., F. Reuter, and J. Vörös, *Review of transducer principles for label-free biomolecular interaction analysis*. Biosensors, 2011. **1**(3): p. 70-92.
85. Ligler, F.S., *Perspective on optical biosensors and integrated sensor systems*. Analytical chemistry, 2009. **81**(2): p. 519-526.
86. Bonanno, L.M. and E. Segal, *Nanostructured porous silicon-polymer-based hybrids: from biosensing to drug delivery*. Nanomedicine, 2011. **6**(10): p. 1755-1770.
87. Bonanno, L.M. and L.A. DeLouise, *Whole blood optical biosensor*. Biosensors and Bioelectronics, 2007. **23**(3): p. 444-448.
88. Thust, M., et al., *Porous silicon as a substrate material for potentiometric biosensors*. Measurement Science and Technology, 1996. **7**(1): p. 26.
89. Dancil, K.-P.S., D.P. Greiner, and M.J. Sailor, *A porous silicon optical biosensor: detection of reversible binding of IgG to a protein A-modified surface*. Journal of the American Chemical Society, 1999. **121**(34): p. 7925-7930.
90. Pacholski, C., *Photonic crystal sensors based on porous silicon*. Sensors, 2013. **13**(4): p. 4694-4713.

91. Kilian, K.A., T. Böcking, and J.J. Gooding, *The importance of surface chemistry in mesoporous materials: lessons from porous silicon biosensors*. Chemical Communications, 2009(6): p. 630-640.
92. Sailor, M.J. and E.C. Wu, *Photoluminescence-based sensing with porous silicon films, microparticles, and nanoparticles*. Advanced Functional Materials, 2009. **19**(20): p. 3195-3208.
93. Jane, A., et al., *Porous silicon biosensors on the advance*. Trends in biotechnology, 2009. **27**(4): p. 230-239.
94. Dhanekar, S. and S. Jain, *Porous silicon biosensor: Current status*. Biosensors and bioelectronics, 2013. **41**: p. 54-64.
95. Bera, B., D. Mandal, and M.D. Sarkar, *Porous silicon and its nanoparticle as biomaterial: A review*. Imperial Journal of Interdisciplinary Research (IJIR), 2016. **2**(11): p. 4.
96. Levoska, J., M. Tyunina, and S. Leppävuori, *Laser ablation deposition of silicon nanostructures*. Nanostructured Materials, 1999. **12**(1-4): p. 101-106.
97. Melikjanyan, G. and K.S. Martirosyan, *Influence of anodization parameters of porous silicon on its glucose sensitivity*. Journal of Contemporary Physics (Armenian Academy of Sciences), 2012. **47**(4): p. 193-195.
98. Hamza, S. and A. Kiani, *A rapid and easy procedure of conductive 3D nanofibrous structure induced by nanosecond laser processing of Si wafer coated by Au thin-film*. Sensing and bio-sensing research, 2017. **16**: p. 6-11.
99. Hamza, S., A. Ignaszak, and A. Kiani, *Synthesis of electrical conductive silica nanofiber/gold nanoparticle composite by laser pulses and sputtering technique*. Nanoscale research letters, 2017. **12**(1): p. 432.
100. Kiani, A., K. Venkatakrishnan, and B. Tan, *Direct laser writing of amorphous silicon on Si-substrate induced by high repetition femtosecond pulses*. Journal of Applied Physics, 2010. **108**(7): p. 074907.
101. Paladiya, C. and A. Kiani, *Synthesis of Silicon Nano-fibrous (SiNf) thin film with controlled thickness and electrical resistivity*. Results in Physics, 2019. **12**: p. 1319-1328.
102. Gamaly, E.G., et al., *Ablation of solids by femtosecond lasers: Ablation mechanism and ablation thresholds for metals and dielectrics*. Physics of plasmas, 2002. **9**(3): p. 949-957.
103. El-Amin, A. and A. Solieman, *Influence of Heat Treatment on the Optical Properties of Thermal Evaporated SnO<sub>2</sub> Thin Films*. Silicon, 2016. **8**(4): p. 517-523.
104. Khan, A.F., et al., *Effect of annealing on electrical resistivity of rf-magnetron sputtered nanostructured SnO<sub>2</sub> thin films*. Applied Surface Science, 2009. **255**(20): p. 8562-8565.
105. De, A. and S. Ray, *A study of the structural and electronic properties of magnetron sputtered tin oxide films*. Journal of Physics D: Applied Physics, 1991. **24**(5): p. 719.
106. Wells, O.C., A. Broers, and C. Bremer, *Method for examining solid specimens with improved resolution in the scanning electron microscope (SEM)*. Applied Physics Letters, 1973. **23**(6): p. 353-355.
107. Goldstein, J.I., et al., *Scanning electron microscopy and X-ray microanalysis*. 2017: Springer.

108. Goehner, R. and J. Michael, *Phase identification in a scanning electron microscope using backscattered electron Kikuchi patterns*. Journal of research of the National Institute of Standards and Technology, 1996. **101**(3): p. 301.
109. Bonse, J., K.-W. Brzezinka, and A. Meixner, *Modifying single-crystalline silicon by femtosecond laser pulses: an analysis by micro Raman spectroscopy, scanning laser microscopy and atomic force microscopy*. Applied surface science, 2004. **221**(1-4): p. 215-230.
110. Baravkar, A., R. Kale, and S. Sawant, *FTIR Spectroscopy: principle, technique and mathematics*. International Journal of Pharma and Bio Sciences, 2011. **2**(1): p. 513-519.
111. Shaikh, T.N. and S. Agrawal, *Qualitative and Quantitative Characterization of Textile Material by Fourier Transform Infra-Red*. IJRSET, 2014. **3**(1): p. 8496.
112. Doyle, W.M., *Principles and applications of Fourier transform infrared (FTIR) process analysis*. Process Control Qual, 1992. **2**(1): p. 11-41.
113. Li, X.-q. and W.-x. Zhang, *Sequestration of metal cations with zerovalent iron nanoparticles a study with high resolution X-ray photoelectron spectroscopy (HR-XPS)*. The Journal of Physical Chemistry C, 2007. **111**(19): p. 6939-6946.
114. Van der Heide, P., *X-ray photoelectron spectroscopy: an introduction to principles and practices*. 2011: John Wiley & Sons.
115. Shallenberger, J., D. Cole, and S. Novak, *Characterization of silicon oxynitride thin films by x-ray photoelectron spectroscopy*. Journal of Vacuum Science & Technology A: Vacuum, Surfaces, and Films, 1999. **17**(4): p. 1086-1090.
116. Hollinger, G., et al., *X-ray photoelectron spectroscopy of thermally grown silicon dioxide films on silicon*. Chemical Physics Letters, 1975. **36**(4): p. 441-445.
117. Azároff, L.V., et al., *X-ray Diffraction*. Vol. 3. 1974: McGraw-Hill New York.
118. Knaepen, W., et al., *In-situ X-ray diffraction study of metal induced crystallization of amorphous silicon*. Thin Solid Films, 2008. **516**(15): p. 4946-4952.
119. Nast, O., et al., *Polycrystalline silicon thin films on glass by aluminum-induced crystallization*. IEEE transactions on electron devices, 1999. **46**(10): p. 2062-2068.
120. Abed, M.M., F. Gaspari, and A. Kiani, *Optical properties of Si/SiO<sub>2</sub> nano structured films induced by laser plasma ionization deposition*. Optics Communications, 2020: p. 125297.
121. Gardelis, S., et al., *Structural and optical characterization of two-dimensional arrays of Si nanocrystals embedded in SiO<sub>2</sub> for photovoltaic applications*. Journal of Applied Physics, 2012. **111**(8): p. 083536.
122. Magnozzi, M., et al., *Optical properties of amorphous SiO<sub>2</sub>-TiO<sub>2</sub> multilayered coatings for 1064-nm mirror technology*. Optical Materials, 2018. **75**: p. 94-101.
123. Liu, H., et al., *Study on SiO<sub>2</sub> thin film modified by post hot isostatic pressing*. Vacuum, 2018. **148**: p. 258-264.
124. Petersen, S., J. Jakobi, and S. Barcikowski, *In situ bioconjugation—novel laser based approach to pure nanoparticle-conjugates*. Applied surface science, 2009. **255**(10): p. 5435-5438.
125. Van Du, N., et al., *Photoluminescence enhancement OF Er<sup>3+</sup>-DOPED ZnO/SiO<sub>2</sub> nanocomposites fabricated through two-step synthesis*. Optical Materials, 2019. **92**: p. 262-266.

126. Besner, S., et al., *Ultrafast laser based “green” synthesis of non-toxic nanoparticles in aqueous solutions*. Applied Physics A, 2008. **93**(4): p. 955-959.
127. Rode, A.V., B. Luther-Davies, and E.G. Gamaly, *Ultrafast ablation with high-pulse-rate lasers. Part II: Experiments on laser deposition of amorphous carbon films*. Journal of Applied Physics, 1999. **85**(8): p. 4222-4230.
128. Šimurka, L., et al., *Mechanical and optical properties of SiO<sub>2</sub> thin films deposited on glass*. Chemical Papers, 2018. **72**(9): p. 2143-2151.
129. Paskaleva, A., E. Atanassova, and G. Beshkov, *The effect of rapid thermal annealing in vacuum on the properties of thin SiO<sub>2</sub> films*. Journal of Physics D: Applied Physics, 1995. **28**(5): p. 906.
130. Alvisi, M., et al., *Deposition of SiO<sub>2</sub> films with high laser damage thresholds by ion-assisted electron-beam evaporation*. Applied Optics, 1999. **38**(7): p. 1237-1243.
131. Ariza-Flores, D., et al., *Design and optimization of antireflecting coatings from nanostructured porous silicon dielectric multilayers*. Solar energy materials and solar cells, 2014. **123**: p. 144-149.
132. Thøgersen, A., J.H. Selj, and E.S. Marstein, *Oxidation effects on graded porous silicon anti-reflection coatings*. Journal of The Electrochemical Society, 2012. **159**(5): p. D276-D281.
133. Bland, H.A., et al., *superconducting Diamond on silicon Nitride for Device Applications*. Scientific reports, 2019. **9**(1): p. 1-9.
134. Niedermeier, M., et al., *Combining mixed titania morphologies into a complex assembly thin film by iterative block-copolymer-based sol-gel templating*. Nanotechnology, 2012. **23**(14): p. 145602.
135. Kiani, A., K. Venkatakrishnan, and B. Tan, *Direct patterning of silicon oxide on Si-substrate induced by femtosecond laser*. Optics express, 2010. **18**(3): p. 1872-1878.
136. Hernández, D., et al., *Emissive properties of SiO<sub>2</sub> thin films through photonic windows*. Applied Physics Letters, 2012. **100**(9): p. 091901.
137. Rodríguez, J.A., et al., *Emission mechanisms of Si nanocrystals and defects in SiO<sub>2</sub> materials*. Journal of Nanomaterials, 2014. **2014**.
138. Koch, F. and V. Petrova-Koch, *Light from Si-nanoparticle systems—a comprehensive view*. Journal of non-crystalline Solids, 1996. **198**: p. 840-846.
139. Dohnalová, K., et al., *White-emitting oxidized silicon nanocrystals: Discontinuity in spectral development with reducing size*. Journal of Applied Physics, 2010. **107**(5): p. 053102.
140. Mahadik, D., et al., *Double layer SiO<sub>2</sub>/Al<sub>2</sub>O<sub>3</sub> high emissivity coatings on stainless steel substrates using simple spray deposition system*. Applied surface science, 2014. **299**: p. 6-11.
141. Iwayama, T., et al., *Enhanced luminescence from encapsulated silicon nanocrystals in SiO<sub>2</sub> with rapid thermal anneal*. Vacuum, 2006. **81**(2): p. 179-185.
142. Yu, H., et al., *Effects of size, shape and floatage of Cu particles on the low infrared emissivity coatings*. Progress in organic Coatings, 2009. **66**(2): p. 161-166.
143. He, X., et al., *High emissivity coatings for high temperature application: progress and prospect*. Thin Solid Films, 2009. **517**(17): p. 5120-5129.
144. Yi, J., et al., *Electron beam-physical vapor deposition of SiC/SiO<sub>2</sub> high emissivity thin film*. Applied surface science, 2007. **253**(9): p. 4361-4366.

- 145 Mehonic, A., et al., *Structural changes and conductance thresholds in metal-free intrinsic SiO<sub>x</sub> resistive random access memory*. Journal of Applied Physics, 2015. 117(12): p. 124505.
- 146 Gao, G., et al., *Influence of KMnO<sub>4</sub> Concentration on Infrared Emissivity of Coatings Formed on TC4 Alloys by Micro-Arc Oxidation*. Materials, 2017. 10(11): p. 1301.
147. Arshavsky-Graham, S., et al., *Porous silicon-based photonic biosensors: Current status and emerging applications*. Analytical chemistry, 2018. **91**(1): p. 441-467.

# Appendix

## Permission for reusing Figure 1-3 ;

RightsLink Printable License

<https://s100.copyright.com/App/PrintableLicenseFrame.jsp?publisherID...>

### ELSEVIER LICENSE TERMS AND CONDITIONS

May 26, 2020

---

---

This Agreement between Ontario tech university -- Meisam Moghareh abed ("You") and Elsevier ("Elsevier") consists of your license details and the terms and conditions provided by Elsevier and Copyright Clearance Center.

License Number	4836750652885
License date	May 26, 2020
Licensed Content Publisher	Elsevier
Licensed Content Publication	Sensors and Actuators B: Chemical
Licensed Content Title	Nano structured sensing surface: Significance in sensor fabrication
Licensed Content Author	Chirag Paladiya,Amirkianoosh Kiani
Licensed Content Date	Sep 1, 2018
Licensed Content Volume	268
Licensed Content Issue	n/a
Licensed Content Pages	18
Start Page	494